



Geochemical and tectonic setting of mafic dike swarms of the Juruena-Teles Pires mineral province, southwestern Amazonian craton, Brazil

Gilmar José Rizzotto^{1*} , Cléber Ladeira Alves¹ 

¹Geological Survey of Brazil (SGB-CPRM), Rua 148, n° 485, Goiânia-GO, Brazil, CEP: 74.170-110

Abstract

The present study provides a comprehensive set of whole-rock geochemical, petrographic, and mineral chemistry data on diabase dike swarms that crosscut the Archean/Paleoproterozoic basement of the Peixoto de Azevedo domain, located in the central-western part of the Juruena-Teles Pires mineral province, in the southwestern portion of the Amazonian craton. The dike swarms are classified into two groups based on TiO₂ concentration: high-Ti (HTi, >2 wt.%) and low-Ti (LTi, <2 wt.%). In the Peixoto de Azevedo domain, LTi dikes, with an undetermined crystallization age, predominantly exhibit N30-40E strikes. In contrast, in the central-western Juruena-Teles Pires province, the ~1.8 Ga fissure-controlled HTi dikes are systematically aligned along shear zones and fault systems, with strikes varying from E-W to WNW-ESE, predominantly crosscutting Orosirian/Statherian granitic rocks. Mineral assemblages in LTi dikes are dominated by clinopyroxene (augite) and plagioclase, the latter sometimes exhibiting a Ca-rich core (An₆₃₋₇₄) and a Na-enriched rim (An₂₆₋₄₃), with minor Fe-Ti oxides, apatite, and biotite. Conversely, HTi dikes contain labradorite, augite (±olivine), magnetite, and ilmenite, with common accessory minerals such as biotite and apatite. Both groups exhibit low Ni contents, which, in conjunction with the observed CaO-MgO correlations, indicate fractional crystallization likely controlled by plagioclase and clinopyroxene. The HTi and LTi dikes are tholeiitic and classified as continental flood basalts, displaying distinct geochemical features. LTi dikes have Mg# values ranging from 0.32 to 0.58 and are enriched in Ba, K, Rb, Sr, Ce, and Y, with low to moderate MgO, Ni, and Cr contents, and moderate LREE enrichment. In contrast, HTi dikes have relatively low Mg# (31–49) and are slightly more evolved than the LTi diabase dikes. Additionally, they exhibit higher concentrations of TiO₂, P₂O₅, Ba, Rb, Sr, Th, Ce, Y, Zr, as well as both LREE and HREE. The relationship between typical crustal elements in the chemical composition of the studied diabases, such as Ba, Rb, La, Ce, and Nb-Ta, supports the presence of a crustal component in the source of both HTi and LTi dikes. These geochemical characteristics suggest that crustal contamination and fractional crystallization may have influenced their magmatic evolution. The probable occurrence of lithospheric delamination, accompanied by crustal thinning and mantle uplift followed by mantle melting, likely culminated in the generation of intraplate continental tholeiitic magmatism, often marking significant geodynamic events in the southwestern portion of the Amazonian craton.

Article Information

Publication type: Research papers
Received 11 September 2024
Accepted 24 March 2025
Online pub. 10 April 2025
Editor : Christophe Renac

Keywords:

Mafic dike swarms
Amazonian craton
High-Ti magmas
Low-Ti magmas
Intraplate magmatism
Paleoproterozoic

*Corresponding author
Gilmar Rizzotto
E-mail address: gilmar.rizzotto@sgb.gov.br

1. Introduction

Mafic dike swarms, recognized as significant tectonic markers and indicators of regional stress regimes, are extensively distributed across the Amazonian craton (Halls 2008; Ernst and Bell 2010; Srivastava 2011; Ernst et al. 2013; Teixeira et al. 2019). Despite their importance, limited studies have focused on the geochemical composition, formation mechanisms, and emplacement processes of the Paleoproterozoic mafic dike swarms, particularly in the

northern Mato Grosso region, within the Juruena-Teles Pires mineral province. These dikes are key representatives of igneous activity associated with major continental rifting and extensional environments, providing pathways to magma ascending. Such magmatic activity is a critical means of tracking periods of continental rifting and supercontinent fragmentation, with magma sources often linked to the subcontinental lithosphere or mantle plumes. In this context, Abbott and Isley (2002) proposed that plume activity between 2.9 and 1.7 Ga profoundly influenced crust-mantle evolution



during the Paleoproterozoic. However, while mantle plumes are recognized as a significant source of mafic magmatism, other tectonic processes, such as plate tectonics and continental rifting, can also generate mafic magmatism. During continental extension, as observed in rifting environments, lithospheric thinning facilitates partial melting of the underlying mantle, leading to the formation of mafic magmas.

At upper crustal levels, mafic dike emplacement and intraplate plutono-volcanism, including bimodal rhyolite/basalt associations, typically accompany lithospheric stretching and rifting. Similarly, in many Large Igneous Provinces, mafic dike swarms frequently act as major components of magmatic conduit systems within continental rifts (Bryan 2007; Ernst et al. 1995; Condie 1995).

In this sense, a significant extension/rifting event occurred during the early Statherian, when a sequence of 1.8 Ga (U-Pb on zircon) igneous rocks, including bimodal plutonic and volcanic rocks, recorded the emplacement of important diabase dike swarms. These swarms are aligned along a N70W to E-W trend, forming the Juruena-Teles Pires province in the southwestern Amazonian craton (Rizzotto et al. 2019). This age coincides with the peak ages reported for magmatism and mineralization in the Juruena-Teles Pires province (Assis et al. 2017). Conversely, gold-mineralized dikes in the Tapajós province yielded an age of approximately 1.89 Ga, interpreted as orogenic and associated with the Ingarana Gabbro (Santos et al. 2002).

This study aims to present new field observations, major and trace element bulk-rock data, and mineral chemistry to elucidate, through geochemical characteristics, the petrogenetic processes and possible emplacement environments of distinct Paleoproterozoic mafic dikes exposed in the southwestern Amazonian craton.

2. Geological setting

The studied region is located in the central-eastern part of the Juruena-Teles Pires mineral province, which is situated in the southwestern portion of the Amazonian craton. It is composed of two major geochronological provinces: the Ventuari-Tapajós (VTP) province in the northeast and the Rio Negro-Juruena province in the central-western region (Tassinari and Macambira, 1999, 2004). The southernmost part of the Ventuari-Tapajós province was defined by Santos et al. (2000, 2004) as Peixoto de Azevedo domain (PAD, 2.1–1.85 Ga; Fig. 1). Within this domain, the Archean basement, exposed as an inlier, is represented by migmatites and orthogneisses attributed to the Córrego Gavião Gneiss (2.8 Ga, Paes de Barros 2007). This older fragment is surrounded by the Cuiú-Cuiú Complex (2.05–1.99 Ga), which consists of tonalitic-granodioritic gneisses intruded by various granitoids forming an extensive calc-alkaline magmatic series linked to a continental magmatic arc. These granitoids include the Pé Quente suite (Assis 2015; Alves et al. 2020) and coeval intermediate to felsic volcanic rocks of the Jarina Formation (2.0–1.97 Ga), as well as the Novo Mundo, Aragão, Nhandu, and Flor da Mata suites (1.97–1.95 Ga; Paes de Barros 2007; Assis 2015; Alves et al. 2020). In addition, younger granitoids belonging to the Guarantã do Norte and Matupá suites (1.90–1.87 Ga), formed in an intraplate extensional environment and are correlated with the Parauari and Maloquinha suites of the VTP.

Regarding mafic magmatism within the PAD, Moura and Botelho (2002) describe two types of diabase dikes (N20E strike) intruding the Matupá suite (1.87 Ga): porphyritic and hypidiomorphic equigranular types, both exhibiting geochemical signatures consistent with intraplate tholeiitic basalts. In the geological context of the Amazonian craton, within the Ventuari-Tapajós province, Santos et al. (2002) identified five basaltic events, two of which are likely correlated with Paleoproterozoic mafic magmatism in the studied area. Those gold-hosting dikes (trending N40E to N60E) yielded an age of 1893 ± 10 Ma (U-Pb on zircon) and are interpreted as being associated with the Ingarana Gabbro (Uatumã SLIP event). Post-orogenic Crepori sills (N55W to N75W strike) yielded an age of 1780 ± 9 Ma (U-Pb on baddeleyite) and are correlated with diabase dike swarms and intrusions (Vespor/Guadalupe suite, 1.78–1.77 Ga, U-Pb on zircon) of the Juruena-Teles Pires mineral province (Rizzotto et al. 2019). In a similar geological context, the northern Amazonian craton (Guiana Shield) exhibits significant intraplate mafic activity, represented by the Avanavero LIP event (1.79 Ga), which comprises mafic dikes and sills (Reis et al. 2013).

The chronostratigraphic positioning of diabase dikes in the PAD remains under investigation. However, these dikes, assigned to the Flor da Serra Suite, crosscut both the entire Cuiú-Cuiú basement and Orosirian granitoids (Alves et al. 2020), suggesting a younger age relative to their host rocks. Conversely, Bispo-Santos et al. (2012) reported diabase dikes and microgabbros, dated at 1.42 Ga ($^{40}\text{Ar}/^{39}\text{Ar}$), that crosscut granites of the Matupá suite, predominantly trending NW-SE, with some displaying a NE-SW orientation.

Westward, the Peixoto de Azevedo domain is bordered, overlain, and intruded by younger rocks (1.82–1.75 Ga, U-Pb on zircon). These consist of subvolcanic and shallow intrusive A-type granitoids, along with coeval felsic volcanic rocks (Colíder group, Teles Pires suite, Juruena supersuite), which are genetically linked to diabase dike swarms and intrusions of the Flor da Serra and Guadalupe suites (Alves et al. 2020; Rizzotto et al. 2019).

Acid magmatism of the Juruena supersuite is extensively developed along a continuous WNW-ESE belt in the central-eastern part of the Juruena-Teles Pires province. It is predominantly represented by granitic bodies, with granodiorites occurring to a lesser extent. The Colíder group is chiefly composed of acid volcanic rocks, including lava flows, lava domes, pyroclastic deposits, and epiclastic rocks. The Teles Pires suite encompasses plutonic rocks and acid subvolcanic intrusions that are temporally, spatially, and genetically associated with the volcanic rocks of the Colíder group (Fig. 1).

Pinho et al. (2003) describe a bimodal volcanic association in the western portion of the Juruena-Teles Pires province, consisting of mafic flows (basalt sill), rhyolite, rhyodacite-dacite occurring as coherent flows, and pyroclastic deposits. Gold mineralization and hydrothermal alteration are closely associated with these volcanic units. U–Pb dating suggests that the volcanic rocks formed within a narrow age range from 1770 ± 6 Ma to 1797 ± 5 Ma, with the latter age interpreted as the crystallization age of the basalt sills.

These units are linked to a Statherian gold metallogenic event, with ore-forming processes temporally correlated with felsic magmatism (Assis et al. 2017).

Therefore, the diabase dike swarms of the Juruena-

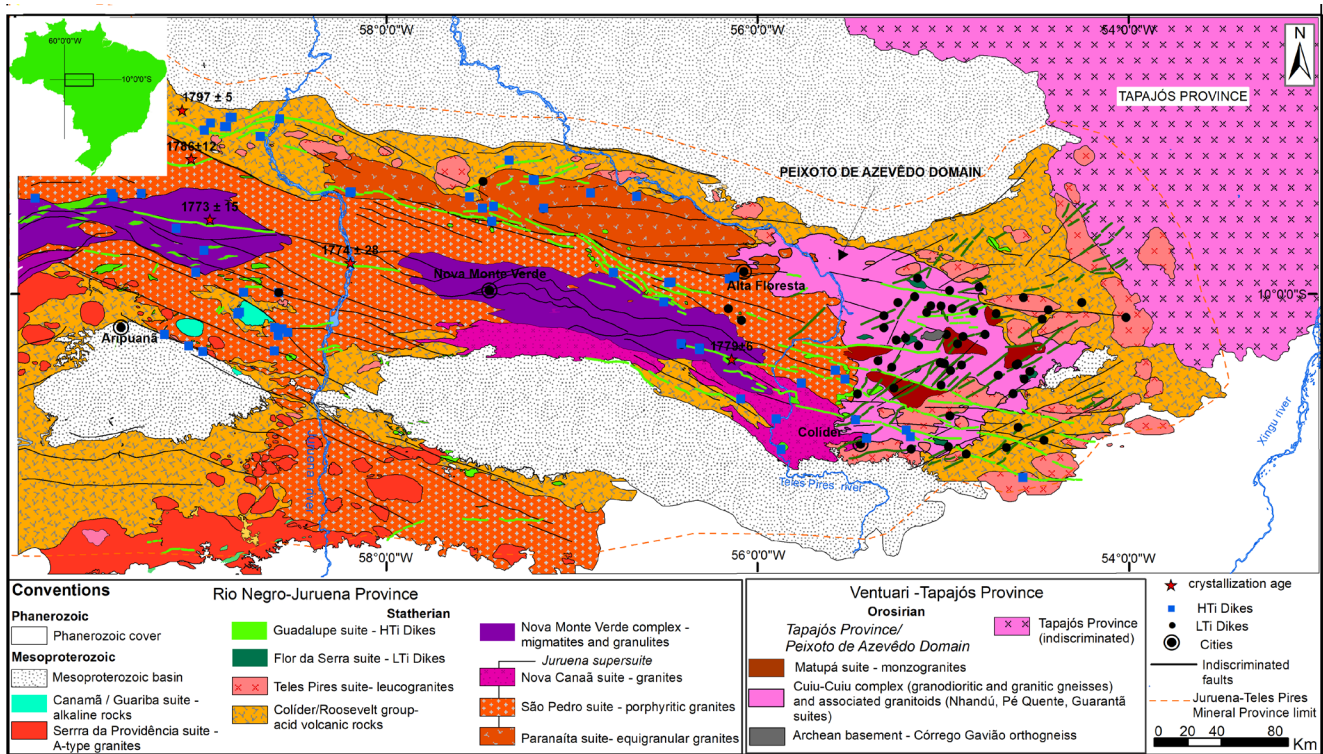


FIGURE 1. Simplified geological map of Juruena-Teles Pires mineral province, showing the oldest terrains: Ventuari-Tapajós province (Peixoto de Azevêdo domain).

Teles Pires province provide valuable insights into the origin and tectonic significance of intraplate igneous activity across vast regions of the southwestern Amazonian craton. These features hold significant implications for understanding the assembly and evolutionary dynamics of the Paleoproterozoic supercontinents.

3. Methods and analytical procedures

This study is based on geological mapping at a 1:100,000 scale, conducted by the Geological Survey of Brazil. Sampling sites are shown in Figure 1 and field aspects of diabase dikes are described in the next section. The microscopic study focused on 78 thin sections from the most representative dike samples in the study area, where textural and mineralogical aspects were characterized in order to reinforce understanding of their genesis.

For the geochemical analysis, the samples were pulverized to a 150-mesh fraction using an agate mill at the Geological Survey of Brazil laboratories. The analyses were performed by SGS Geosol laboratories, Brazil, on 69 samples of the diabase dikes, which showed no significant evidence of post-magmatic alteration. Major elements were obtained by X-ray fluorescence spectrometry after a lithium tetraborate fusion followed by nitric acid digestion for sample preparation. Trace elements were determined by ICP-MS (Inductively Coupled Plasma Mass Spectrometer) following a lithium metaborate fusion and multiacid digestion (1HCl/1HNO₃/1HF/1HClO₄). Loss on ignition (LOI) was measured after ignition at 405°C and/or 1000°C. The litho geochemistry results were processed by GeoChemical Data Toolkit 4.1 (GCDkit) software. The detailed analytical procedures are available on <http://www.sgsgeosol.com.br>.

Mineral chemical analyses of mafic rocks were performed on polished thin sections of clinopyroxene, amphibole, plagioclase, ilmenite and magnetite using a JEOL JXA-8230 EPMA five-spectrometer electron microprobe at the Estadual Paulista University (UNESP). The analytical conditions were an accelerating voltage of 15 kV and a beam current of 20 nA. The beam diameter used was between 5 and 10 µm. The elements analyzed and their standards were as follows: Na (albite), Mg (olivine), Al (anorthite), Si (orthoclase), K (orthoclase), Ca (wollastonite), Ti (ilmenite), Cr (chromite), Mn (rhodonite) and Fe (ilmenite). All analytical X-ray lines were K alpha; counting times were 20s for both peaks and backgrounds.

4. Field relationships of the diabase dikes

The dikes are primarily distributed within the Peixoto de Azevedo domain, although the longest ones (ranging from tens of meters to a few kilometers) are found in the central-eastern portion of the Juruena-Teles Pires mineral province, specifically between the Juruena and Xingu rivers (Fig. 1). In this region, the dikes are dominantly composed of basalt, with andesitic basalt occurring less frequently. Some dikes extend over 200 km in length, typically exhibiting a subvertical, tabular geometry. Their widths generally do not exceed 30 m, with predominant orientations ranging from E-W to WNW-ESE (Fig. 2 and Table 2). These dikes were emplaced along shear zones, faults, and fracture systems in pre-existing zones of weakness. In addition, they exhibit evidence of hybridization with coeval acidic rocks, represented by the granites of the São Pedro, Paranaíta, and Teles Pires suites, as well as the Colider Volcanics (Fig. 3). Evidence of mutually cross-cutting

relationships between the dikes and the host intrusives, along with features such as rounded boundaries and injection veinlets at the contact, suggests that both magmas were partially molten, classifying the dikes as synplutonic. In this context, small subcircular gabbro and microgabbro bodies (Vespor and Guadalupe suites) are commonly found, typically associated with the intersections of extensional structures trending E-W, from which some diabase dikes radiate. Furthermore, the presence of mafic microgranular enclaves within the granites of the aforementioned suites facilitated the formation of narrow hybrid rock zones, represented by granodiorites (Rizzotto et al. 2019). When cutting through volcanic rocks, the dynamic spatial behavior of the dikes becomes evident as they branch into smaller segments before coalescing into a single, continuous feature. They exhibit abrupt contacts with the surrounding granitic rocks and lack metamorphism. However, they occasionally show signs of

hydrothermal alteration, resulting in a mineral paragenesis dominated by actinolite, epidote, and chlorite.

Due to rare outcrops and high weathering rates, with granitic, volcanic, and mafic rocks capped by thick laterite, determining the relative ages of dike swarms based on mutual intersections was not possible. Only two intersections of diabase dikes with rhyolites from the Colider group were observed. In one case, the rhyolite cuts the diabase dike (N70W strike), while in the other, the rhyolite is cut by a diabase dike (E-W). This suggests recurring episodes of basic and acidic magmatism or that both types were largely contemporaneous in the central part of the Juruena-Teles Pires mineral province.

In the Peixoto de Azevedo domain, the dikes are discontinuous, rarely exceeding 30 km in length, and are predominantly composed of diabase. They follow two preferential orientations: NE-SW and WNW-ESE, with the latter being less frequent (Fig. 1 and Table 2). Andesitic,

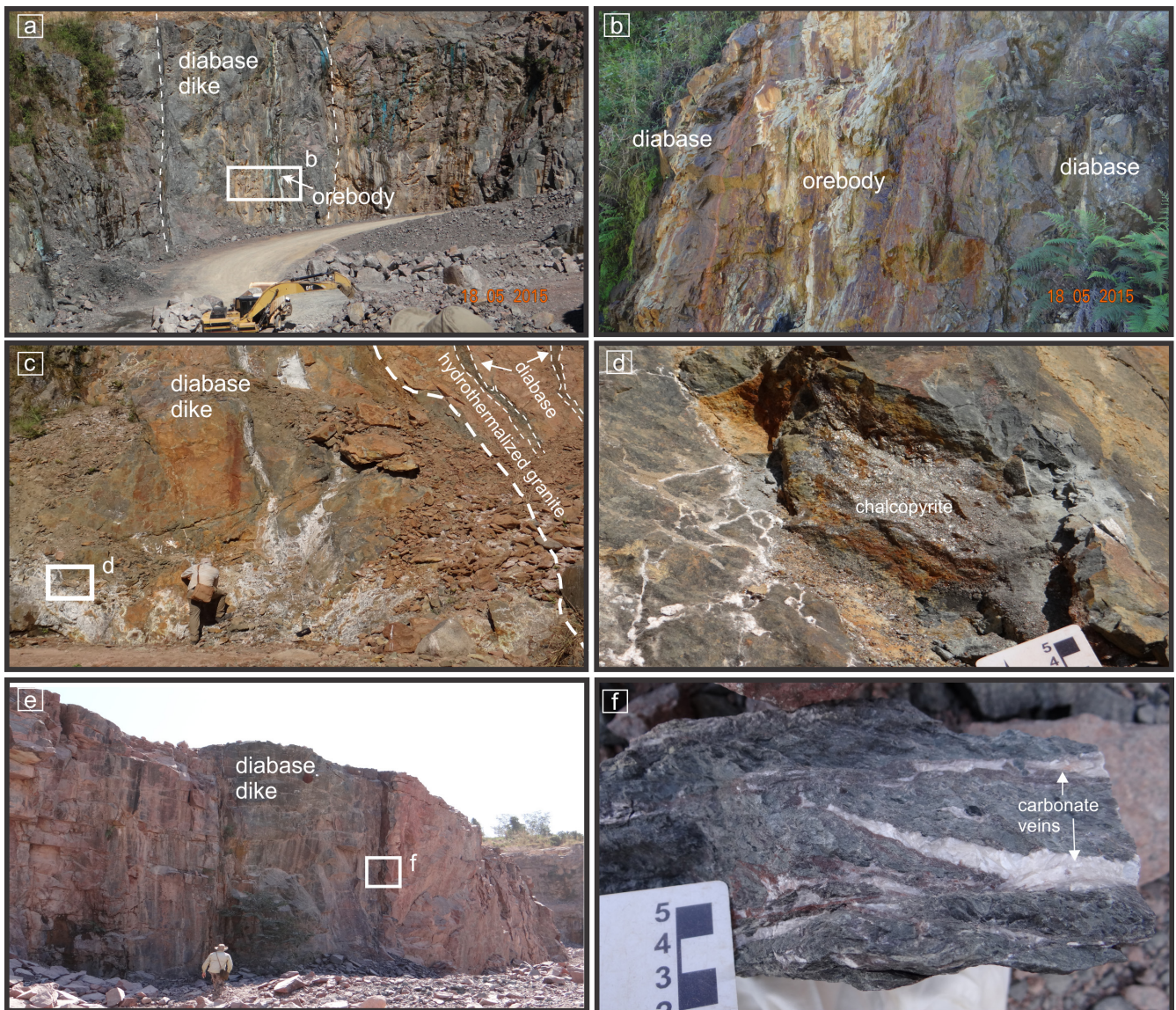


FIGURE 2. Mesoscopic features of mafic dikes and their surrounding rocks. (a) A vertical NE-SW trending diabase dike, cross-cutting tonalitic rock. (b) Detail of an orebody with leached Cu- and Fe-bearing sulfides. (c) A diabase dike cross-cutting hydrothermally altered granite of the Carol-Mila deposit. (d) Detail of a chalcopyrite pocket and leached sulfide veinlets (white color) inside the diabase. (e) An E-W-trending diabase dike cutting the Teles Pires granite. Detail of the contact zone between the dike and granite, showing strong hydrothermal alteration forming calcite veins.

dacitic, and rhyolitic dikes are of limited occurrence, narrow, and discontinuous, making detailed mapping unfeasible. All dikes cross-cut the Cuiú-Cuiú basement rocks and granitoids of the Orosirian suites. However, their contact relationships are not well-defined, leaving their chronostratigraphic positioning uncertain. Additionally, no isotopic data are available. In general, most NE-SW-striking dikes exhibit hydrothermal alteration, resulting in the formation of hydrated mineral paragenesis (actinolite, epidote, chlorite, \pm calcite) and Fe- and Cu-bearing sulfides. This group of dikes shares similar structural trends with most of the Au-bearing veins and is parallel to the ore vein contacts (Fig. 2). However, a genetic link is not necessarily implied, as many dikes are barren. Nonetheless, metallogenetic studies by Alves et al. (2019) on 41 artisanal gold mines in the Peixoto de Azevedo domain identified an association between mafic dikes and quartz-gold-bearing veins.

U-Pb datings (determined by LA-ICPMS on zircon) from gabbro bodies and dikes of the Vespôr (or Guadalupe) suite in the central-western portion of the Juruena-Teles Pires province yielded ages of 1773 ± 15 , 1774 ± 28 , 1797 ± 5 and 1786 ± 12 Ma (Ribeiro and Duarte 2010; Pinho et al. 2003). East of the Juruena river, Rizzotto et al. (2019) dated a porphyritic gabbro, which yielded an age of 1779 ± 6 Ma (U-Pb on zircon). A diabase dike branches out from this intrusion, following a N70W to E-W trend. These ages, ranging from 1797 to 1773 Ma, indicate the emplacement timing of the mafic dike swarm

(N70W to E-W trends) in the central-eastern Juruena-Teles Pires mineral province.

5. Petrography

Based on field characteristics, petrographic studies, and the abundance of the major elements (e.g., SiO_2 and MgO), the diabase dikes can be divided into two groups, as discussed in Section 7, based on their TiO_2 content: high-Ti (HTi) dikes ($>2\%$ TiO_2) and low-Ti (LTi) dikes ($<2\%$ TiO_2).

The HTi dikes, trending N70W to E-W, are associated with the stratigraphic context of the Guadalupe/Vespôr suite. They are predominantly distributed in the central-western region of the Juruena-Teles Pires mineral province, with a preference for this area, though occasional occurrences are also observed in the Peixoto de Azevêdo domain (Fig. 1). Conversely, the LTi group, trending from N30E to N40E, is primarily located in the Peixoto de Azevêdo domain, forming the dominant group, which accounts for 70% of the studied samples. This group belongs to the Flor da Serra suite.

Most LTi basic dikes exhibit a subophitic texture and are fine- to medium-grained. Ophitic and porphyritic textures are rare, with the dominant phenocrysts consisting mainly of idiomorphic and hypidiomorphic plagioclase (An_{57-74}) and rare clinopyroxene (Fig. 4a, 4b). Clinopyroxene is represented by augite. Euhedral primary iron oxides (mainly magnetite and/or ilmenite) are also present, along with apatite and biotite as



FIGURE 3. Features of mixing between coexisting magmas. (a) Breached and magmatic mafic microgranular enclaves forming hybrid rocks. (b) Evidence of magma mixing between mafic rock (dark grey) and granite (light grey). (c) A magmatic enclave containing K-feldspar xenocrysts derived from the surrounding magma. (d) Pyrite veinlets in hybrid rock.

accessory minerals. Hydrothermal alteration products include actinolite, chlorite, epidote, Fe/Cu sulfides, white mica, and iron oxides/hydroxides. Actinolite generally forms at clinopyroxene edges, while epidote and white mica occur in the cores of prismatic plagioclase crystals. Symplectitic quartz-feldspar intergrowths are rare. Some LTI dikes near gold orebodies exhibit weak pyritization, including the formation of pyrite stringers.

The HTi dikes exhibit a dominant subophitic texture, are medium-grained, and contain plagioclase, clinopyroxene, and magnetite/ilmenite as the primary minerals, with smaller amounts of olivine (Fig. 4c, 4d). Olivine phenocrysts, when present, are intensely altered to iddingsite and/or bowlingite. Clinopyroxene occurs as prismatic phenocrysts, as well as zoned and twinned microphenocrysts. Zoned prismatic plagioclase crystals are also present. Most of the HTi dikes are fresh or weakly altered, with sericite, chlorite, and epidote as the main hydrothermal minerals.

6. Mineral chemistry

6.1. Clinopyroxene

Clinopyroxene in the LTI diabase dikes has been identified as augite. However, one subgroup exhibits higher CaO and lower MgO and FeO contents (En_{39-43} , Wo_{39-44} , Fs_{15-17}) compared to another subgroup (En_{40-50} , Wo_{32-40} , Fs_{15-20} ; Fig. 5a). Zoned clinopyroxene phenocrysts are rare but commonly have MgO-rich cores with FeO_{\pm} and CaO-rich rims (Table 1a). Clinopyroxene in the HTi dikes has a more restricted compositional range (En_{41-44} , Wo_{37-40} , Fs_{18-19}) compared to that in the LTI dikes. The average crystallization temperature of clinopyroxene is 1117°C, based on the Wang et al. (2021) thermometer.

6.2. Plagioclase

Plagioclase in LTI diabase dikes generally shows zoning, with Ca-rich cores (An_{63-74}) and Na-enriched rims (An_{26-43}), indicating chemical instability within the magma chamber. In nearly all LTI diabase dike samples, plagioclase is identified as labradorite (An_{52-69}). However, in four samples, it is classified as bytownite (An_{71-74} ; Fig. 5b). The HTi diabase dikes, in turn, exhibit a more restricted plagioclase composition, classified as labradorite (An_{50-59}). Although rare zoned crystals are present, they display Na-enriched rims (An_{23-38}). The crystallization temperature of plagioclase was determined using the Kudo and Weill (1970) thermometer, assuming anhydrous conditions. The average temperature obtained was 1197°C.

6.3. Magnetite/Ilmenite

Magnetite is the predominant opaque mineral in LTI diabase dikes, with ilmenite and ulvöspinel occurring less frequently, often as exsolution phases within magnetite. Similarly, in HTi diabase dikes, ilmenite is the dominant exsolution phase in magnetite, occurring as scarce lamellae within or at the rims of host magnetite, while ulvöspinel is rarely observed. The TiO_2 content in magnetite from LTI diabase dikes displays a broad compositional range, varying from 6.51% to 16.30%, whereas in HTi diabase dikes, it is more constrained, ranging from 12.90% to 15.33%. The TiO_2 content in ilmenite from HTi dikes ranges from 48.58% to 49.30%. In contrast, the ulvöspinel content is relatively low, around 2.20%.

6.4. Amphibole

Hydrothermal greenish amphiboles are present in a few diabase dike samples, predominantly in LTI dikes, with rare occurrences in HTi dikes.

According to Hawthorne et al. (2012) classification, these amphiboles are identified as actinolite (Fig. 5c), with a magnesium number (Mg#) between 0.64 and 0.71, low TiO_2 , and high Al_2O_3 contents. Although amphibole crystals are generally unzoned, they occasionally exhibit lamellar intergrowths between actinolite and tremolite. These two amphiboles are rarely found together, forming a patchy intergrowth that may be easily overlooked.

7. Whole-rock Geochemistry

The analytical data are reported in Table 2. Samples that were identified with cumulus mineral phases, based on textural and chemical criteria, such as low Al_2O_3 ($\leq 12\%$) and high MgO ($>9.5\%$), were excluded from geochemical treatment. All analyzed samples, including both LTI and HTi diabase dikes, exhibit a tholeiitic affiliation. The majority are classified as basalts, while basaltic andesites are comparatively rare, and restricted to a few LTI dike samples (Fig. 6).

In the bivariate variation diagram of Mg# (molar $Mg/(Mg+Fe^{2+})$) versus TiO_2 (Figs. 7a, b) the diabase dikes are classified into two groups based on TiO_2 concentration, with values higher or lower than 2 wt.%, corresponding to HTi and LTI dikes, respectively. Both groups exhibit a typical tholeiitic differentiation trend, where Fe_2O_3 and TiO_2 increase as MgO decreases. As discussed below, the two groups also differ in other geochemical characteristics.

7.1 LTI Dikes

Mg# values range from 0.32 to 0.58. With decreasing Mg# values, Al_2O_3 , CaO, Ni, and Cr contents show a corresponding decrease, while SiO_2 , FeO , TiO_2 , and P_2O_5 concentrations increase. However, alkalis (Na_2O and K_2O) show a dispersed pattern. This elemental behavior suggests that fractionation was primarily controlled by the crystallization of plagioclase and clinopyroxene. The notably steeper decline of Cr compared to Ni with decreasing Mg#, along with the negative correlation between Ca and Al, suggest clinopyroxene fractionation (Figs. 7a-b). Plagioclase fractionation is evidenced by the constant Sr behavior throughout differentiation, as well as small negative Eu anomalies in several samples (Table 2). The incompatible elements Rb, Ba, Sr, Ce, and Y exhibit a moderate to weak increase with decreasing Mg#, further supporting the role of plagioclase and augite in magma differentiation (Fig. 7b). Furthermore, TiO_2 and P_2O_5 concentrations increase with decreasing Mg#, indicating that during fractional crystallization, minerals such as clinopyroxene and plagioclase extract Mg, Ca, and other compatible elements, leading to the enrichment of incompatible elements (e.g., Ti, P) in the residual melt. In contrast, most LILEs (e.g. La, Ce, Nd, Rb, Ba, K) exhibit a wide compositional range for a given Mg#, suggesting that their distribution was influenced by additional processes, including possible crustal contamination (Figs. 7b and 8).

The REE patterns of LTI dikes indicate high variability in incompatible elements. They display a moderately

TABLE 1. (a) Representative electron microprobe analyses of clinopyroxene.

SAM- PLE	DF48 c1-1	DF48 c1-2	DF48 c1-3	DF48 c1-5	DF48 c4-1	DF48 c4-2	DF48 c4-3	DF48 c4-4	DF48 c1-4	DF192 c1-1	DF192 c1-2	DF192 c1-3	DF192 c1-4	DF192 c1-6	DF177 c1-1	DF177 c1-2	DF177 c1-3	DF177 c1-4	DF177 c1-5	DF177 c3-1	DF177 c3-2	DF177 c3-3	DF177 c3-4	DF177 c3-5	DF92 c3-2	DF92 c3-4
SiO ₂ (wt.%)	49.32	48.52	50.24	48.33	49.94	51.10	51.19	48.83	47.66	49.29	48.76	50.13	50.64	50.25	52.15	49.79	50.21	46.48	49.96	50.19	49.19	49.00	49.96	49.84	50.32	51.02
TiO ₂	1.20	1.27	0.73	1.37	1.23	0.84	0.76	1.19	1.15	1.34	1.48	1.12	1.00	1.04	0.38	0.75	0.73	0.67	0.66	0.73	0.68	0.86	0.72	0.64	0.66	0.52
Al ₂ O ₃	3.43	4.54	2.36	4.53	3.90	1.91	2.38	4.14	4.21	3.68	4.11	2.79	2.62	2.86	1.94	4.13	3.15	3.03	3.69	2.71	3.79	3.98	3.39	3.01	3.30	1.91
FeOt	10.50	10.15	9.61	10.74	10.50	11.05	9.66	10.33	10.00	11.46	11.02	11.14	11.07	11.58	10.62	9.45	11.46	10.15	9.76	12.71	11.00	9.76	9.50	9.90	8.79	13.03
MgO	14.05	13.79	15.07	13.76	14.40	14.81	14.96	14.00	12.80	14.22	13.82	14.63	14.75	15.01	17.84	15.07	15.01	13.92	15.19	14.95	16.18	14.98	15.20	14.92	15.97	15.41
MnO	0.29	0.22	0.25	0.25	0.22	0.33	0.24	0.22	0.23	0.27	0.25	0.25	0.25	0.27	0.30	0.24	0.31	0.25	0.25	0.35	0.28	0.21	0.24	0.25	0.22	0.42
Cr ₂ O ₃	L.D.L	0.09	0.08	0.05	L.D.L	L.D.L	0.03	0.02	0.08	0.04	0.03	0.02	0.03	0.03	0.17	0.29	0.03	0.09	0.24	L.D.L	0.24	0.24	0.10	0.08	0.48	0.01
CaO	19.93	20.65	19.57	19.48	19.85	19.14	20.06	20.36	20.13	18.42	19.10	19.18	18.82	17.85	16.09	19.49	17.99	21.42	19.38	17.20	16.81	19.18	19.50	19.39	19.21	17.05
Na ₂ O	0.44	0.45	0.36	0.44	0.51	0.38	0.35	0.42	0.46	0.41	0.44	0.40	0.31	0.32	0.20	0.28	0.29	0.31	0.30	0.27	0.29	0.25	0.30	0.30	0.25	0.29
Total	99.2	99.7	98.3	99.0	100.5	99.6	99.6	99.5	96.7	99.1	99.0	99.7	99.5	99.2	99.7	99.5	99.2	96.3	99.4	99.1	98.5	98.5	98.9	98.3	99.2	99.7
Si	1.854	1.812	1.896	1.82	1.85	1.91	1.91	1.83	1.84	1.71	1.84	1.88	1.90	1.89	1.93	1.85	1.88	1.79	1.86	1.89	1.85	1.85	1.87	1.88	1.87	1.91
Al _{IV}	0.146	0.188	0.104	0.18	0.15	0.08	0.09	0.17	0.16	0.17	0.16	0.12	0.10	0.11	0.07	0.15	0.12	0.14	0.14	0.11	0.15	0.15	0.13	0.12	0.13	0.08
Total	2.00	2.00	2.00	2.00	2.00	2.00	2.00	2.00	2.00	1.88	2.00	2.00	2.00	2.00	2.00	2.00	2.00	1.93	2.00	2.00	2.00	2.00	2.00	2.00	2.00	2.00
Al _{VI}	0.005	0.011	0.001	0.02	0.02	0.00	0.01	0.01	0.03	0.00	0.02	0.00	0.01	0.02	0.01	0.04	0.02	0.00	0.02	0.01	0.02	0.02	0.02	0.01	0.02	0.00
Ti	0.034	0.036	0.021	0.04	0.03	0.02	0.02	0.03	0.03	0.04	0.04	0.03	0.03	0.03	0.01	0.02	0.02	0.02	0.02	0.02	0.02	0.02	0.02	0.02	0.02	0.01
Fe ₊₃	0.11	0.14	0.09	0.11	0.11	0.07	0.06	0.13	0.10	0.36	0.09	0.09	0.05	0.06	0.05	0.08	0.07	0.26	0.09	0.07	0.11	0.10	0.09	0.09	0.08	0.08
Mg	0.79	0.77	0.85	0.77	0.79	0.83	0.83	0.78	0.74	0.85	0.78	0.82	0.82	0.84	0.983	0.84	0.84	0.80	0.84	0.84	0.91	0.84	0.85	0.839	0.89	0.86
Fe ₊₂	0.21	0.17	0.20	0.21	0.20	0.26	0.23	0.18	0.21	0.01	0.25	0.24	0.28	0.28	0.25	0.20	0.27	0.07	0.20	0.31	0.21	0.20	0.19	0.21	0.18	0.30
Ca	0.80	0.83	0.79	0.79	0.79	0.77	0.80	0.82	0.83	0.80	0.77	0.77	0.76	0.72	0.64	0.78	0.72	0.89	0.77	0.69	0.68	0.77	0.78	0.78	0.77	0.68
Na	0.03	0.03	0.03	0.03	0.04	0.03	0.03	0.03	0.03	0.03	0.03	0.03	0.02	0.02	0.01	0.02	0.02	0.02	0.02	0.02	0.02	0.02	0.02	0.02	0.02	0.02
Total	1.98	1.98	1.98	1.98	1.98	1.98	1.98	1.98	1.98	2.10	1.98	1.98	1.97	1.97	1.96	1.97	1.97	2.05	1.97	1.97	1.96	1.97	1.97	1.97	1.96	1.97
Wo	41.82	43.24	40.74	41.43	41.28	39.57	41.42	42.52	44.03	39.07	40.70	39.78	39.21	37.37	32.70	40.74	37.62	43.97	40.26	35.89	35.09	40.26	40.57	40.52	39.78	35.04
En	40.99	40.17	43.65	40.74	41.67	42.60	43.00	40.65	38.92	41.96	40.97	42.20	42.78	43.70	50.45	43.85	43.67	39.76	43.91	43.41	46.99	43.75	44.00	43.35	46.01	44.07
Fs	17.20	16.59	15.61	17.84	17.05	17.83	15.58	16.84	17.05	18.97	18.33	18.02	18.01	18.93	16.85	15.41	18.71	16.26	15.83	20.70	17.92	15.99	15.43	16.13	14.21	20.89

FeOt= total iron on
FeO

LDL = lower than detection limit.

Number of ions on the basis of 6 (O)

TABLE 1. (b) Representative electron microprobe analyses of plagioclase.

SAM- PLE	DF48 c2-1R	DF48 c2-2	DF48 c2-3	DF48 c2-4	DF48 c2- -5R	DF192 c3-1	DF192 c3-2	DF192 c3-3	DF192 c3- -4R	DF192 c4-1	DF192 c4-2	DF192 c4-3	DF192 c4-4	DF192 c4-5	DF92 c1-1	DF92 c1-2R	DF92 c1-3	DF92 c1-4	DF92 c2-1	DF92 c2- -2R	DF92 c2-3	DF92 c2-4	DF177 c2-1	DF177 c2-2	DF177 c2-3	DF177 c2-4	DF177 c2-5	DF177 c4- -1R	DF177 c4- -2R	DF177 c4- -3R
SiO2 (wt.%)	61.70	50.20	50.47	51.39	56.06	53.16	52.42	52.57	55.26	54.26	54.73	53.75	53.44	53.43	51.75	56.49	52.70	51.89	52.60	58.01	53.56	52.79	50.35	49.49	49.65	50.50	49.68	51.71	51.63	52.18
Al2O3	24.34	31.68	30.89	30.43	27.50	29.13	29.59	29.39	27.54	28.12	28.41	29.25	29.18	28.89	30.18	26.45	29.60	29.53	29.90	26.58	29.08	28.88	30.85	31.69	31.70	31.21	31.93	30.30	29.86	29.53
FeOt	0.85	0.66	0.66	0.75	0.80	0.58	0.51	0.48	0.55	0.56	0.60	0.58	0.58	0.61	0.76	0.67	0.97	0.92	0.77	0.55	0.79	0.89	0.68	0.61	0.61	0.70	0.66	0.83	0.86	0.94
MgO	0.04	0.06	0.11	0.09	0.09	0.05	0.04	0.05	0.08	0.06	0.06	0.07	0.08	0.06	0.18	0.08	0.20	0.17	0.14	0.04	0.13	0.11	0.22	0.19	0.22	0.21	0.23	0.18	0.16	0.15
CaO	5.40	14.62	14.03	13.51	9.96	12.05	12.54	12.08	10.01	10.52	10.90	11.93	11.80	11.82	13.41	8.90	12.25	12.39	12.92	8.45	11.89	12.23	14.30	15.20	15.03	14.59	15.26	13.46	13.05	12.49
Na2O	7.93	3.14	3.53	3.89	5.78	4.41	4.36	4.33	5.21	4.96	5.11	4.46	4.50	4.53	3.82	6.19	4.29	3.95	4.03	6.35	4.51	4.40	3.31	2.96	3.01	3.25	2.88	3.74	4.01	4.12
K2O	1.06	0.15	0.18	0.16	0.34	0.52	0.45	0.57	0.84	0.52	0.42	0.55	0.45	0.49	0.28	0.41	0.33	0.74	0.33	0.73	0.38	0.37	0.14	0.11	0.12	0.14	0.11	0.19	0.21	0.23
BaO	0.40	0.00	0.06	0.06	0.07	0.07	0.06	0.07	0.02	0.01	0.01	0.03	0.02	0.06	L.D.L	0.08	0.02	0.03	0.01	0.06	0.02	0.04	0.05	L.D.L	L.D.L	0.03	L.D.L	L.D.L	L.D.L	0.03
Total	101.7	100.5	99.9	100.3	100.6	100.0	100.0	99.5	99.5	99.0	100.2	100.6	100.0	99.9	100.4	99.3	100.4	99.6	100.7	100.8	100.3	99.7	99.9	100.3	100.3	100.6	100.8	100.4	99.8	99.7
Si	10.84	9.12	9.20	9.32	10.05	9.12	9.51	9.58	10.03	9.91	9.87	9.69	9.68	9.70	9.38	10.23	9.53	9.47	9.50	10.34	9.68	9.61	9.19	9.01	9.03	9.16	9.01	9.38	9.41	9.52
Al	5.04	6.78	6.64	6.51	5.81	6.23	6.33	6.31	5.89	6.05	6.04	6.21	6.23	6.18	6.44	5.64	6.31	6.35	6.36	5.58	6.19	6.20	6.64	6.80	6.80	6.67	6.82	6.48	6.41	6.35
Fe	0.12	0.10	0.10	0.11	0.12	0.09	0.08	0.07	0.08	0.09	0.09	0.09	0.09	0.09	0.12	0.10	0.15	0.14	0.12	0.08	0.12	0.14	0.10	0.09	0.09	0.11	0.10	0.13	0.13	0.14
Ca	1.02	2.84	2.74	2.63	1.91	2.34	2.44	2.36	1.95	2.06	2.11	2.30	2.29	2.30	2.60	1.73	2.37	2.42	2.50	1.61	2.30	2.39	2.80	2.97	2.93	2.83	2.97	2.61	2.55	2.44
Na	2.70	1.11	1.25	1.37	2.01	1.55	1.53	1.53	1.83	1.76	1.79	1.56	1.58	1.59	1.34	2.17	1.50	1.40	1.41	2.20	1.58	1.55	1.17	1.05	1.06	1.14	1.01	1.31	1.41	1.46
K	0.24	0.03	0.04	0.04	0.08	0.12	0.10	0.13	0.19	0.12	0.09	0.13	0.10	0.12	0.06	0.09	0.08	0.17	0.08	0.17	0.09	0.09	0.03	0.03	0.03	0.03	0.03	0.04	0.05	0.05
Total	19.96	19.99	19.97	19.97	19.97	19.45	19.98	19.98	19.98	19.98	19.99	19.98	19.98	19.98	19.95	19.98	19.95	19.95	19.96	19.99	19.96	19.97	19.94	19.95	19.94	19.94	19.94	19.95	19.96	19.96
Ab	68.29	27.74	30.98	33.94	50.23	38.65	37.63	38.07	46.13	44.62	44.81	39.02	39.76	39.74	33.47	54.40	38.04	35.01	35.39	55.22	39.83	38.54	29.28	25.89	26.43	28.43	25.30	33.10	35.24	36.87
An	25.70	71.38	68.04	65.14	47.83	58.35	59.81	58.64	48.98	52.30	52.82	57.81	57.62	57.37	64.92	43.23	60.03	60.68	62.70	40.60	58.02	59.33	69.90	73.47	72.88	70.76	74.07	65.79	63.54	61.77
Or	6.01	0.87	0.98	0.92	1.94	3.00	2.56	3.30	4.89	3.08	2.37	3.17	2.62	2.89	1.61	2.37	1.93	4.32	1.91	4.18	2.15	2.14	0.81	0.63	0.69	0.81	0.64	1.11	1.22	1.35

TABLE 1. (c) Representative electron microprobe analyses of amphibole.

SAMPLE	SiO2	TiO2	Al2O3	FeOt	MgO	MnO	CaO	Na2O	K2O	Total	Si	AlIV	Total	AlVI	Ti	Mg	Fe+2	Total	Ca	Na	K	Total
DF48c1-1	51.49	L.D.L	2.07	13.67	14.78	0.23	12.19	0.21	0.18	94.83	7.7	0.3	8	0.07	0	3.3	1.63	5	1.89	0.06	0.04	1.99
DF48c1-2	53.73	0.026	1.11	13.32	15.23	0.26	12.62	0.19	0.02	96.51	7.86	0.14	8	0.05	0	3.32	1.63	5	1.96	0.05	0	2.01
DF48c1-3	52.3	0.201	2.97	13.71	14.99	0.24	12.07	0.14	0.02	96.65	7.65	0.35	8	0.16	0.02	3.27	1.55	5	1.85	0.04	0	1.89

Cations calculated on the bases of 23 oxygens

Oxides in wt. %

TABLE 1. (d) Representative electron microprobe analyses of Fe-Ti oxides.

MINERAL	MAGNETITE													ILMENITE			
	DF92 c5_1	DF92 c5_2	DF92 c5_3	DF92 c5_4	DF92 c5_5	DF92 c5_6	DF177 c4_1	DF177 c4_2	DF48 c5_1	DF48 c5_2	DF48 c5_4	DF192 c5_1	DF192 c5_3	DF192 c5_4	DF177 c4_3	DF48 c5_3	DF192 c5_2
SiO ₂	3.28	11.12	0.08	0.07	0.28	0.32	0.11	0.11	0.09	0.09	0.08	0.09	0.10	L.D.L	5.53	0.01	L.D.L
Al ₂ O ₃	0.19	1.20	0.08	0.05	0.33	0.32	0.09	0.10	0.06	0.08	0.20	2.75	2.94	0.09	1.47	0.01	0.05
TiO ₂	6.51	11.63	17.20	16.11	24.51	23.64	14.87	15.18	14.85	14.48	16.37	12.92	15.33	48.58	35.90	49.57	49.30
FeOt	82.84	60.86	76.35	77.78	66.48	67.64	78.85	78.76	79.02	79.99	77.32	78.35	75.94	49.07	50.36	46.73	48.48
MgO	0.04	0.52	0.01	0.01	0.05	0.07	0.06	0.06	0.04	0.04	0.04	0.35	0.45	0.45	1.78	0.04	0.39
MnO	0.38	0.01	1.90	1.81	2.68	2.73	1.03	0.98	1.07	1.08	1.22	0.23	0.29	0.81	2.51	3.43	0.76
Cr ₂ O ₃	0.01	0.03	0.04	0.03	0.02	0.03	0.08	0.08	0.05	0.06	0.16	0.24	0.22	0.03	0.02	0.01	0.05
CaO	2.63	9.79	0.14	0.21	0.10	0.10	0.04	0.03	0.03	0.01	0.01	0.01	0.01	0.00	0.33	0.00	0.01
K ₂ O	0.00	0.02	L.D.L	L.D.L	0.02	0.02	0.00	0.01	0.00	0.01	0.00	L.D.L	L.D.L	0.01	0.03	L.D.L	0.01
Total	95.87	95.18	95.81	96.06	94.48	94.88	95.13	95.31	95.20	95.82	95.40	94.94	95.28	99.05	97.92	99.80	99.05
Si	0.12	0.40	0.00	0.00	0.01	0.01	0.00	0.00	0.00	0.00	0.00	0.00	0.00	0.00	0.20	0.00	0.00
Ti	0.18	0.31	0.49	0.46	0.72	0.69	0.43	0.44	0.43	0.41	0.47	0.37	0.43	1.39	0.99	1.41	1.41
Al	0.01	0.05	0.00	0.00	0.02	0.01	0.00	0.00	0.00	0.00	0.01	0.12	0.13	0.00	0.06	0.00	0.00
Fe ³⁺	1.39	0.52	1.00	1.07	0.53	0.58	1.13	1.11	1.13	1.16	1.04	1.13	0.99	-0.78	-0.46	-0.82	-0.82
Fe ²⁺	1.18	1.31	1.43	1.40	1.63	1.60	1.39	1.40	1.39	1.38	1.43	1.34	1.40	2.33	2.01	2.30	2.36
Cr	0.00	0.00	0.00	0.00	0.00	0.00	0.00	0.00	0.00	0.00	0.00	0.01	0.01	0.00	0.00	0.00	0.00
Mn	0.01	0.00	0.06	0.06	0.09	0.09	0.03	0.03	0.03	0.03	0.04	0.01	0.01	0.03	0.08	0.11	0.02
Mg	0.00	0.03	0.00	0.00	0.00	0.00	0.00	0.00	0.00	0.00	0.00	0.02	0.03	0.03	0.10	0.00	0.02
Ca	0.10	0.38	0.01	0.01	0.00	0.00	0.00	0.00	0.00	0.00	0.00	0.00	0.00	0.00	0.01	0.00	0.00
Total	3.00	3.00	3.00	3.00	3.00	3.00	3.00	3.00	3.00	3.00	3.00	3.00	3.00	3.00	3.00	3.00	3.00
Ulvo-spinel	2.23	2.16	2.29	2.28	2.34	2.32	2.30	2.30	2.30	2.28	2.30	2.27	2.26	2.28	2.21	2.27	2.28
FeO (%)	38.11	43.56	44.83	43.99	50.21	49.57	43.56	43.95	43.55	43.46	44.80	42.54	44.56	73.59	65.27	72.68	74.35
Fe ₂ O ₃ (%)	49.70	19.23	35.03	37.55	18.08	20.08	39.22	38.69	39.42	40.60	36.14	39.75	34.87	-27.26	-16.57	-28.85	-28.75
Total	100.77	97.07	99.26	99.79	96.26	96.84	98.98	99.10	99.10	99.82	98.84	98.62	98.52	96.28	96.23	96.88	96.09

Structural formula based on 4 oxygen

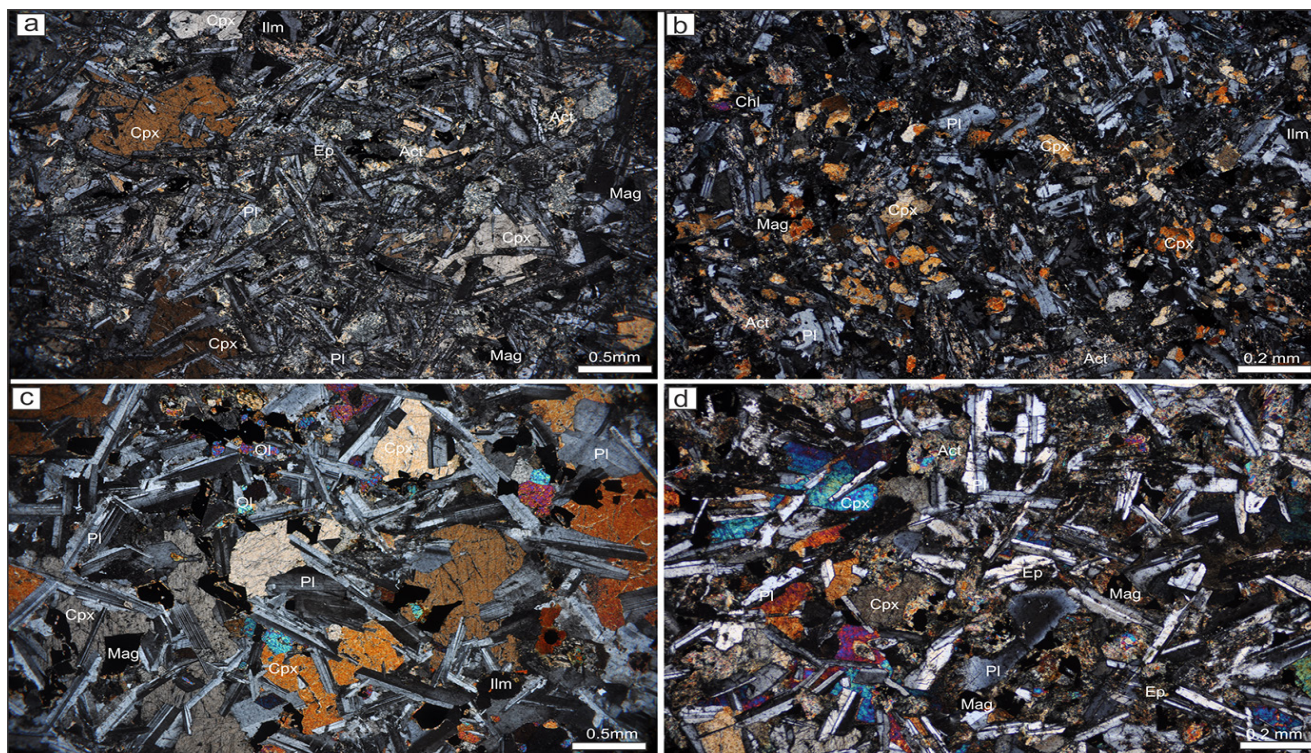


FIGURE 4. (a) Photomicrographs highlighting the textural features of diabase dikes: LTI dikes (a, b) and HTi dikes (c, d) under cross-polarized light. Abbreviations: Cpx-clinopyroxene; Ol-olivine; Pl-plagioclase; Act-actinolite; Mag-magnetite; Ilm-ilmenite; Ep-epidote; Chl-chlorite.

fractionated REE pattern relative to chondrite (Nakamura 1974), with moderate to strong enrichment in LREE (30x to 90x chondrite) and a $(La/Sm)_{cn}$ ratio of 0.79 to 3.82 (Fig. 9 and Table 2). There is also weak enrichment of HREE (~8x chondrite) with a $(Gd/Yb)_{cn}$ ratio of 1.27 to 2.49. Eu anomalies are minor, ranging from weakly negative to weakly positive ($Eu/Eu^*=0.80$ to 1.16; Fig. 9a).

In the primitive mantle-normalized diagram (Sun and McDonough 1989), LTI dikes exhibit moderate negative Nb, Ta, and Ti anomalies, along with weak positive Th, La, Ce, and Nd anomalies. Compared to HTi dikes, they show slightly stronger negative Nb and Ti anomalies. This geochemical pattern is similar to that of continental flood basalts, which also display negative Nb-Ta anomalies and strong enrichment in incompatible elements (Fig. 9b).

7.2 HTi Dikes

The HTi diabase dikes have a narrower Mg# range (0.31-0.49) and are slightly more evolved than the LTI diabase dikes. However, five HTi dike samples have Mg# values ranging from 0.52 to 0.58, suggesting variable degrees of fractional crystallization. The HTi dikes follow and extend the LTI dike variation trends for most major elements (Fig. 7a). For a given Mg#, they show higher concentrations of TiO_2 , P_2O_5 , Ba, Rb, Sr, Th, Ce, Y, Zr, as well as LREE and HREE (Figs. 7b and 9a). This strong fractionation appears to be a characteristic feature of continental tholeiites. In the REE chondrite-normalized diagram, as well as the primitive mantle-normalized trace element diagram, HTi dikes exhibit strong LREE enrichment (70x to 150x chondrite) with a $(La/Sm)_{cn}$ ratio of 0.88 to 2.72.

They also show moderate HREE enrichment (~25x chondrite), with a $(Gd/Yb)_{cn}$ ratio of 1.55 to 2.01 (Fig. 9a), and a weak or absent negative Eu anomaly ($Eu/Eu^*=0.85$ to 1.18). In the primitive mantle-normalized diagram (Fig. 9b), HTi dikes display weak negative Nb, Ta, and Ti anomalies, along with weak to moderate positive Th, La, Ce, and Nd anomalies. Only two samples exhibit a different geochemical behavior, resembling the LTI patterns.

8. Discussion

We first examine the geochemical imprint of fractional crystallization and/or crustal contamination processes, demonstrating that these mechanisms account for the incompatible element variations observed between the LTI and HTi diabase dike swarms in the Jurueña-Teles Pires mineral province.

In the context of fractional crystallization, the variation in incompatible element ratios becomes evident as Mg# decreases. Along this trend, Al_2O_3 , CaO, Ni, and Cr decline, while SiO_2 , FeO, Na_2O , K_2O , P_2O_5 , and all incompatible trace elements increase, indicating the fractional crystallization of plagioclase and augite (\pm olivine). Additionally, the significant decrease in Ni and Cr abundances suggests that the fractional crystallization of clinopyroxene (\pm olivine) played a key role in the evolution of the diabase dikes.

The increase in TiO_2 , FeO, and P_2O_5 , with the decrease in Mg# suggests late-stage crystallization of Fe-Ti oxide minerals (ilmenite and/or titanomagnetite) and apatite. This pattern is characteristic of tholeiitic magmas in the intermediate to late stages of differentiation, where fractional crystallization plays

TABLE 2. Representative major (wt.%) and trace element (ppm) concentrations, along with significant element ratios, for diabase dikes. Major elements oxides are reported in wt.%. Mg# is calculated as molar Mg/(Mg+Fe²⁺), assuming Fe₂O₃/FeO= 0.15. The last row of the table, displays the strike values of selected diabase dikes.

SAMPLE	B4 121	B4 150	B4 169	B4 192	B4 60	CA-145	CA-268	CA-34	CA-40C	CA-42	CA-479	CA-545B
SiO ₂	44.89	48.43	46.28	45.37	49.96	47.20	51.10	46.70	46.70	45.80	48.00	52.00
TiO ₂	1.78	1.93	1.75	1.76	1.90	2.61	1.59	1.49	1.36	1.43	2.20	0.75
Al ₂ O ₃	15.75	14.84	15.75	15.88	15.30	16.40	13.30	16.10	15.90	16.10	13.50	16.50
Fe ₂ O ₃	13.38	12.44	14.90	12.71	12.31	14.40	14.40	13.80	13.00	13.00	16.90	9.99
MnO	0.22	0.20	0.38	0.27	0.20	0.19	0.22	0.18	0.19	0.18	0.23	0.19
MgO	7.25	6.99	8.19	8.29	7.47	4.76	4.75	7.27	7.93	8.23	9.32	7.23
CaO	7.52	8.51	4.71	5.34	7.58	7.78	7.19	9.26	9.50	9.96	6.90	10.40
Na ₂ O	3.83	2.46	4.36	3.68	2.75	3.59	2.73	2.43	2.17	1.94	2.51	3.24
K ₂ O	0.54	0.83	0.31	0.59	0.97	1.92	2.42	0.68	1.10	1.03	1.34	1.00
P ₂ O ₅	0.28	0.21	0.38	0.30	0.23	0.51	0.32	0.34	0.22	0.27	0.41	0.19
LOI	3.52	3.28	2.76	3.42	0.01	1.82	1.87	1.55	2.26	2.91	0.55	0.07
Total	99.0	100.1	99.8	97.6	98.7	101.2	99.9	99.8	100.3	100.9	101.9	101.6
Mg#	0.51	0.52	0.51	0.56	0.54	0.39	0.39	0.51	0.54	0.55	0.52	0.58
Ba	543	525	157	376	573	562	1064	609	387	389	598	406
Cu	12.00	31.00	14.00	9.00	23.00	39.30	47.80	80.60	68.20	82.80	38.40	37.30
Ni	47.00	48.00	80.00	101.00	55.00	54.50	15.40	112.00	123.00	155.00	165.60	57.70
Rb	11.00	23.00	4.60	10.00	24.00	76.10	66.30	11.40	52.90	34.40	39.00	31.60
Sr	719.00	854.00	212.00	504.00	758.00	287.00	487.00	490.30	506.80	592.30	313.00	416.00
Y	22.00	31.20	23.00	23.20	26.00	31.30	28.46	21.32	18.87	17.82	32.04	17.93
Zr	111.00	263.00	136.00	147.00	176.00	106.00	178.00	108.40	138.10	103.50	191.00	82.00
Th	0.90	3.18	1.19	1.12	2.79	3.70	6.50	0.90	0.70	0.80	15.70	8.30
Hf	3.20	7.40	3.40	3.80	4.90	4.38	4.56	1.95	2.08	2.26	8.67	4.47
Cs	0.80	1.50	0.90	0.90	1.55	1.70	0.55	0.63	0.88	0.50	1.71	0.53
Nb	10.00	13.20	13.00	10.90	12.10	9.82	5.39	3.40	4.00	3.70	9.31	6.78
Ga	20.00	21.00	19.00	20.00	21.00	19.90	20.10	19.40	19.30	19.00	19.50	15.90
Ta	0.57	0.86	0.61	0.85	0.82	0.26	0.23	0.27	0.36	0.17	1.46	0.76
U	0.29	0.95	0.31	0.30	0.73	0.77	1.04	0.11	0.13	0.16	0.91	0.41
La	20.90	31.10	21.40	20.10	27.50	24.20	32.30	13.10	10.20	12.20	25.30	15.50
Ce	50.00	71.60	53.40	50.80	64.60	54.20	64.00	24.40	25.90	28.60	52.40	33.40
Pr	6.96	8.78	7.65	6.77	7.94	7.23	7.77	3.40	3.73	3.97	6.48	4.02
Nd	32.80	40.70	35.10	32.10	36.10	30.30	33.10	15.90	16.90	18.00	26.80	17.00
Sm	7.08	8.62	7.00	7.04	7.72	6.10	6.30	4.00	4.20	4.20	5.70	3.60
Eu	2.19	2.91	2.10	1.94	2.50	1.91	1.77	1.55	1.50	1.44	1.96	1.27
Gd	5.94	7.09	5.87	5.69	6.37	6.60	6.12	4.53	4.30	4.41	6.35	3.64
Tb	0.87	0.88	0.87	0.88	0.87	0.91	0.85	0.70	0.64	0.62	0.88	0.57
Dy	4.47	4.70	4.57	4.59	4.47	5.92	5.45	4.35	4.00	3.71	5.91	3.36
Ho	0.84	0.87	0.86	0.88	0.84	1.08	1.05	0.84	0.74	0.73	1.21	0.73
Er	2.36	2.44	2.38	2.39	2.36	3.27	3.07	2.44	2.20	1.97	3.42	2.05
Tm	0.32	0.42	0.33	0.36	0.32	0.38	0.41	0.33	0.28	0.26	0.51	0.29
Yb	1.90	2.00	2.00	1.90	1.80	3.10	2.80	2.10	1.90	1.70	3.10	1.80
Lu	0.28	0.32	0.31	0.31	0.28	0.36	0.41	0.28	0.25	0.22	0.52	0.25
La/Sm _{cn}	1.82	2.22	1.88	1.76	2.19	2.44	3.15	2.02	1.49	1.79	2.73	2.65
Gd/Yb _{cn}	3.52	4.39	3.65	3.53	4.32	3.67	5.28	2.89	2.37	2.77	3.98	4.26
Eu/Eu*	1.04	1.14	1.01	0.94	1.10	0.93	0.88	1.12	1.09	1.03	1.00	1.08
strike							N40E		N52E	N15E	N80W	

TABLE 2. (Continued)

SAMPLE	CA-565	CA68B	CA-78B	CA-90B	DF-036	DF-092	DF-134	DF-16	DF-169	DF-134I	DF-17	DF-177
SiO ₂	48.90	46.10	50.00	47.70	51.00	51.50	47.70	48.10	47.00	47.70	48.30	47.30
TiO ₂	3.60	1.47	1.57	1.03	2.07	1.19	1.52	1.92	2.35	2.10	2.25	2.03
Al ₂ O ₃	13.50	16.40	14.20	15.90	13.20	14.90	13.90	17.40	16.90	15.50	17.40	15.80
Fe ₂ O ₃	16.80	13.30	14.90	11.70	15.20	11.50	15.10	11.80	10.80	12.10	11.80	11.90
MnO	0.27	0.18	0.23	0.17	0.24	0.18	0.25	0.16	0.15	0.18	0.16	0.19
MgO	4.81	8.21	5.90	8.00	3.98	5.99	7.21	7.86	6.50	7.77	7.97	8.31
CaO	9.27	9.77	9.26	10.50	7.72	8.94	10.60	9.72	9.86	10.10	9.85	10.60
Na ₂ O	2.81	2.48	2.56	2.00	2.92	2.55	1.77	2.53	3.63	2.23	2.53	2.69
K ₂ O	0.68	0.54	1.40	0.89	1.92	1.33	0.82	0.63	0.86	0.66	0.58	0.68
P ₂ O ₅	0.39	0.28	0.29	0.17	1.09	0.21	0.21	0.15	0.46	0.17	0.15	0.14
LOI	0.28	1.34	0.94	1.73	1.28	1.87	0.98	1.20	2.51	1.94	1.59	2.02
Total	101.3	100.1	101.3	99.8	100.6	100.2	100.1	101.5	101.0	100.5	102.6	101.7
Mg#	0.36	0.55	0.44	0.57	0.34	0.50	0.48	0.57	0.54	0.56	0.57	0.58
Ba	212	332	482	281	934	586	115	224	582	304	205	260
Cu	547.40	75.30	90.00	76.70	11.40	40.50	114.50	102.60	59.90	0.00	78.90	0.00
Ni	57.40	144.00	52.00	109.00	7.30	42.90	79.00	152.00	102.60	62.00	138.00	0.00
Rb	15.80	7.60	24.60	40.70	54.10	42.60	47.30	11.30	26.10	33.40	9.50	20.60
Sr	249.00	622.40	324.60	404.70	583.00	485.00	236.20	351.50	838.00	440.00	325.00	407.00
Y	45.54	18.88	29.84	15.25	30.62	22.68	27.32	19.43	18.73	18.69	18.11	18.59
Zr	268.00	100.90	101.40	104.30	202.00	125.00	107.80	102.40	193.00	102.20	135.50	106.00
Th	8.60	0.90	1.30	1.20	4.40	2.40	1.70	1.10	1.10	0.90	1.00	1.30
Hf	7.37	2.44	0.00	1.76	4.85	3.58	1.73	2.11	4.89	2.30	3.43	2.16
Cs	0.29	0.32	0.62	2.20	2.44	1.26	5.32	1.78	0.86	1.27	0.81	0.99
Nb	17.25	8.60	4.50	9.90	7.82	5.53	12.20	6.70	9.91	3.14	6.10	2.81
Ga	23.50	19.50	0.00	15.50	19.50	18.90	17.20	18.80	17.40	18.20	17.80	17.10
Ta	0.86	1.32	0.36	1.19	0.81	0.45	0.86	1.06	0.33	0.25	0.53	0.28
U	0.58	0.12	0.22	0.10	0.87	0.52	0.22	0.33	0.34	0.15	0.34	0.14
La	20.30	12.10	15.80	11.10	37.10	18.40	11.80	16.80	25.20	11.70	17.00	19.90
Ce	48.50	27.40	33.50	19.20	82.50	41.80	17.70	22.30	49.10	21.60	20.90	19.30
Pr	6.90	3.89	5.12	2.66	5.63	5.46	2.57	2.93	6.59	2.92	2.77	2.59
Nd	31.90	18.40	22.20	12.40	44.40	22.50	12.50	13.50	28.10	13.20	12.60	12.00
Sm	8.40	4.40	5.10	2.90	8.60	4.50	3.50	3.40	5.20	3.20	3.10	2.80
Eu	2.75	1.47	1.64	0.96	2.60	1.49	1.21	1.22	1.71	1.11	1.19	1.01
Gd	9.88	4.58	5.89	3.16	7.88	4.67	4.48	3.89	4.75	3.41	3.60	3.46
Tb	1.41	0.67	0.89	0.49	1.09	0.73	0.77	0.61	0.64	0.53	0.61	0.53
Dy	8.62	3.92	5.48	3.02	6.42	4.43	4.86	3.82	3.85	3.49	3.62	3.49
Ho	1.67	0.76	1.12	0.61	1.23	0.90	1.03	0.80	0.76	0.69	0.76	0.71
Er	4.68	2.14	3.20	1.80	3.65	2.59	3.03	2.26	2.19	2.08	2.13	2.01
Tm	0.67	0.29	0.47	0.25	0.45	0.34	0.43	0.32	0.29	0.29	0.29	0.28
Yb	4.10	1.80	3.00	1.70	3.00	2.40	2.80	2.10	1.80	1.90	1.90	2.00
Lu	0.55	0.25	0.44	0.24	0.46	0.35	0.41	0.29	0.27	0.28	0.26	0.28
La/Sm _{cn}	1.49	1.69	1.91	2.36	2.65	2.52	2.07	3.04	2.98	2.25	3.37	4.37
Gd/Yb _{cn}	2.05	2.64	2.68	3.51	4.71	3.94	2.63	4.32	5.31	3.43	4.72	5.75
Eu/Eu*	0.93	1.01	0.92	0.98	0.97	1.00	0.94	1.03	1.06	1.03	1.10	1.00
strike		N46E		N47E			N68W	N73W	N80W	N83W	N70W	N78W

TABLE 2. (Continued)

SAMPLE	DF-192	DF-203	DF-223	DF-35	DF-48	DF-486	FD-035	FD-06C	FS-08	FS-10 A	FS-12 B	FS-31
SiO ₂	47.80	48.60	44.80	46.70	47.10	45.20	49.70	53.10	45.40	47.20	46.90	49.30
TiO ₂	2.70	1.62	1.68	1.44	1.52	1.95	2.23	0.83	1.54	1.99	1.54	1.73
Al ₂ O ₃	14.80	15.10	16.20	16.10	16.10	15.60	13.20	17.80	16.20	15.30	15.00	14.10
Fe ₂ O ₃	17.20	13.90	14.20	14.00	13.90	14.20	17.80	10.90	13.90	16.40	15.40	15.10
MnO	0.22	0.21	0.19	0.20	0.20	0.19	0.27	0.36	0.19	0.24	0.20	0.22
MgO	6.56	5.72	7.89	7.39	7.27	6.94	4.03	4.79	7.68	5.92	7.05	5.14
CaO	7.57	8.46	9.29	9.09	9.40	8.61	6.88	2.17	10.10	9.56	9.42	8.43
Na ₂ O	3.00	2.92	2.26	2.55	2.64	2.74	2.60	4.48	2.27	2.51	2.36	2.35
K ₂ O	1.68	1.59	1.26	1.17	0.91	1.18	2.23	2.83	0.82	1.06	0.98	1.54
P ₂ O ₅	0.53	0.45	0.29	0.32	0.34	0.39	0.49	0.35	0.28	0.29	0.36	0.63
LOI	0.45	1.54	1.83	1.80	1.72	2.63	3.10	0.20	2.74	1.30	1.85	1.79
Total	102.5	100.1	99.9	100.8	101.1	99.6	102.5	97.8	101.1	101.8	101.1	100.3
Mg#	0.43	0.45	0.52	0.51	0.51	0.49	0.31	0.46	0.52	0.41	0.47	0.40
Ba	565	1592	468	589	596	459	1106	1181	318	609	597	659
Cu	0.00	0.00	0.00	0.00	0.00	57.00	70.70	100.80	99.00	130.90	129.10	71.70
Ni	16.00	21.00	83.00	56.00	42.00	103.00	15.90	50.20	109.00	57.00	119.00	27.00
Rb	41.80	48.10	57.30	60.40	43.30	75.00	48.30	107.70	34.90	53.90	25.10	52.90
Sr	268.00	500.00	635.00	514.00	474.00	644.10	510.00	853.50	664.80	364.60	513.20	481.20
Y	34.43	23.63	18.34	20.85	21.49	23.67	0.00	0.00	22.36	34.83	22.38	28.64
Zr	186.00	104.00	104.00	103.10	109.00	129.20	189.50	147.90	119.40	112.70	101.80	156.00
Th	3.70	1.60	0.70	1.30	0.70	1.20	5.30	4.50	1.10	1.20	1.30	4.10
Hf	5.08	2.86	3.08	2.02	2.05	3.55	4.93	3.01	3.27	3.20	2.22	4.10
Cs	0.96	0.71	2.27	4.50	6.98	4.77	1.33	2.20	0.58	1.09	0.50	0.51
Nb	11.19	3.38	5.21	2.13	1.88	7.04	6.91	6.78	6.30	3.70	7.60	6.90
Ga	20.00	19.40	20.30	19.10	19.20	24.80	29.10	23.40	20.50	22.90	19.80	20.80
Ta	0.97	0.23	0.24	0.37	0.27	0.49	0.53	0.66	1.28	0.78	0.96	0.58
U	0.97	0.38	0.18	0.13	0.12	0.26	0.82	0.98	0.25	0.26	0.22	0.68
La	26.50	16.40	12.80	17.30	12.30	18.00	31.40	31.00	17.80	18.00	18.40	31.30
Ce	55.30	36.90	28.20	21.90	22.60	41.30	66.20	63.70	34.20	30.60	40.30	67.30
Pr	7.16	4.87	4.07	3.19	3.19	5.62	8.49	7.35	4.80	4.33	5.61	8.66
Nd	31.00	21.40	18.80	15.20	15.40	25.70	35.70	31.60	22.00	20.30	24.40	36.10
Sm	6.80	4.50	4.30	3.40	3.40	5.80	7.50	4.60	5.20	5.50	5.40	7.20
Eu	2.02	1.79	1.44	1.39	1.39	1.79	2.39	1.41	1.71	1.99	1.76	2.18
Gd	6.89	4.76	4.37	4.15	4.14	5.78	7.89	4.48	5.36	6.67	5.39	7.03
Tb	1.08	0.76	0.67	0.61	0.63	0.63	1.10	0.45	0.82	1.10	0.78	1.03
Dy	6.76	4.59	3.81	4.18	4.00	4.89	6.87	3.01	4.67	6.73	4.47	5.80
Ho	1.35	0.90	0.76	0.82	0.83	0.89	1.43	0.57	0.92	1.38	0.90	1.13
Er	3.92	2.70	2.00	2.41	2.45	2.48	4.21	1.53	2.49	3.97	2.53	3.21
Tm	0.54	0.36	0.27	0.33	0.31	0.32	0.53	0.31	0.35	0.55	0.33	0.43
Yb	3.40	2.30	1.80	2.00	2.10	2.20	3.70	1.60	2.10	3.60	2.20	2.90
Lu	0.54	0.35	0.26	0.30	0.31	0.27	0.63	0.27	0.31	0.52	0.28	0.40
La/Sm _{cn}	2.40	2.24	1.83	3.13	2.23	1.91	2.58	4.15	2.11	2.01	2.10	2.67
Gd/Yb _{cn}	3.85	3.45	2.93	4.17	2.97	3.11	3.98	6.92	3.32	2.70	3.41	4.45
Eu/Eu*	0.91	1.19	1.02	1.14	1.14	0.95	0.96	0.96	1.00	1.01	1.00	0.94
strike						N51E			N45E	N35E		

TABLE 2. (Continued)

SAMPLE	FS-32	FS-34	FS-44	FS-63	FS-65B	GG-49	GG-77	GG-97 B	GR-101	MA 20A	GR-162	GR-94
SiO ₂	45.50	45.10	50.50	47.10	45.80	48.30	51.70	48.10	49.30	44.49	52.60	49.70
TiO ₂	1.45	1.45	2.62	2.79	1.43	1.30	1.89	1.36	1.30	2.01	0.87	1.27
Al ₂ O ₃	15.10	16.30	16.60	13.60	16.30	16.50	13.40	15.80	15.20	13.36	15.80	14.20
Fe ₂ O ₃	13.40	13.50	13.60	15.60	12.90	14.00	16.40	13.00	12.30	19.14	10.50	12.20
MnO	0.19	0.18	0.19	0.20	0.18	0.19	0.24	0.21	0.18	0.30	0.16	0.43
MgO	8.18	7.98	3.28	4.73	8.06	7.84	5.31	7.73	7.26	6.24	5.92	5.95
CaO	9.53	9.53	7.80	7.57	9.47	9.90	8.96	9.16	3.98	9.97	8.57	7.59
Na ₂ O	1.91	2.16	3.09	3.96	1.88	2.36	2.41	1.97	4.71	2.35	3.19	3.35
K ₂ O	1.17	1.32	2.22	1.58	1.32	0.59	1.23	1.08	3.05	0.89	1.43	2.53
P ₂ O ₅	0.29	0.29	0.57	0.61	0.29	0.23	0.33	0.12	0.26	0.13	0.18	0.29
LOI	2.62	2.62	0.80	1.31	2.56	0.15	0.15	2.37	1.36	0.90	0.86	1.32
Total	99.3	100.4	101.3	99.0	100.2	101.4	102.0	100.9	98.9	99.8	100.1	98.8
Mg#	0.54	0.54	0.32	0.37	0.55	0.52	0.39	0.54	0.54	0.39	0.52	0.48
Ba	474	397	739	893	402	304	529	369	601	246	669	735
Cu	85.70	124.00	79.30	40.50	69.20	160.00	139.00	78.90	10.70	0.00	71.80	95.20
Ni	150.00	141.00	21.00	26.00	139.00	165.00	51.00	110.00	36.00	82.00	60.00	34.00
Rb	60.00	96.70	65.40	21.80	123.60	11.30	32.00	64.90	203.80	35.30	45.10	130.70
Sr	657.30	609.30	377.10	362.20	633.80	215.60	257.20	354.70	268.00	314.80	518.10	452.80
Y	20.33	31.25	42.12	33.62	20.28	19.86	30.32	22.90	27.31	32.40	19.99	26.51
Zr	103.70	105.70	230.30	237.00	102.70	221.30	170.60	104.10	145.30	139.80	104.30	152.70
Th	0.80	0.80	5.70	2.10	1.20	1.50	3.10	2.30	3.30	0.30	3.10	4.70
Hf	2.81	2.86	6.07	5.56	2.55	3.38	4.58	2.87	4.25	2.40	2.79	3.88
Cs	0.99	5.11	2.99	0.38	4.34	1.42	0.79	1.14	18.54	1.20	0.63	4.59
Nb	5.10	5.70	15.40	14.90	8.20	5.90	8.85	5.80	8.20	4.40	5.00	7.30
Ga	20.10	20.20	22.90	22.70	20.10	16.60	20.20	19.00	20.90	23.20	17.70	18.90
Ta	1.41	0.89	1.25	0.95	0.55	0.63	0.59	0.99	0.87	0.00	0.58	1.03
U	0.16	0.16	1.40	0.56	0.17	0.35	0.64	0.23	2.91	0.10	0.46	0.57
La	15.00	16.60	37.40	28.00	13.40	16.90	33.70	14.70	31.70	13.30	22.20	30.20
Ce	34.20	34.20	74.70	58.40	31.40	26.50	49.90	25.60	51.00	13.90	38.60	54.10
Pr	4.86	4.90	9.71	7.94	4.36	3.21	6.03	3.33	6.32	2.19	4.73	6.58
Nd	22.00	22.50	40.10	37.30	20.50	14.70	26.40	15.00	26.20	10.90	19.60	28.20
Sm	5.20	5.30	9.00	8.50	4.70	3.40	5.70	3.80	5.10	3.50	3.90	5.80
Eu	1.63	1.71	2.57	3.00	1.58	1.14	1.77	1.19	1.57	0.00	1.21	1.59
Gd	5.11	5.87	9.09	8.46	4.89	3.94	6.26	4.28	4.93	4.57	3.74	5.43
Tb	0.76	0.88	1.40	1.20	0.72	0.61	0.95	0.67	0.77	0.98	0.59	0.81
Dy	4.14	4.90	8.11	7.26	4.32	3.95	5.86	4.39	4.88	5.53	3.73	4.93
Ho	0.82	1.02	1.70	1.38	0.82	0.77	1.23	0.89	1.03	1.14	0.75	1.02
Er	2.27	2.87	4.77	3.75	2.28	2.36	3.54	2.60	3.10	3.41	2.26	2.92
Tm	0.33	0.37	0.70	0.52	0.30	0.33	0.50	0.36	0.43	0.51	0.29	0.38
Yb	2.00	2.30	4.50	3.30	2.00	2.20	3.30	2.50	2.70	3.45	2.00	2.40
Lu	0.28	0.31	0.63	0.44	0.27	0.30	0.47	0.34	0.40	0.50	0.30	0.36
La/Sm _{cn}	1.77	1.93	2.56	2.03	1.75	3.06	3.64	2.38	3.82	2.34	3.50	3.20
Gd/Yb _{cn}	2.94	2.83	4.11	3.31	2.74	4.29	5.38	3.43	6.43	2.91	5.94	5.56
Eu/Eu*	0.97	0.94	0.87	1.09	1.01	0.96	0.91	0.91	0.96	0.00	0.97	0.87
strike	N43E	N30E			N24E	N30E			N44E			

TABLE 2. (Continued)

SAMPLE	LL-072	TD-156	LM-76B	MA 19A	PS-013	PS-028	PS-241	PS-261	PV-093	TD-080	TD-084	TD-090A
SiO ₂	48.50	47.60	46.52	45.60	52.63	49.50	50.31	46.30	48.60	48.60	48.20	49.00
TiO ₂	2.14	3.34	1.36	1.52	1.51	0.87	1.42	0.94	0.99	2.12	3.49	2.87
Al ₂ O ₃	12.70	13.10	15.70	15.88	16.16	14.22	15.69	17.61	16.90	12.60	13.10	13.90
Fe ₂ O ₃	17.80	16.20	14.46	14.12	12.33	12.21	12.01	13.10	11.20	17.10	15.80	15.60
MnO	0.24	0.27	0.20	0.19	0.17	0.22	0.13	0.14	0.17	0.24	0.25	0.21
MgO	4.41	5.02	5.26	7.18	2.94	7.64	7.05	5.51	7.35	4.06	5.15	5.50
CaO	7.96	8.96	8.66	9.52	7.72	10.68	9.26	10.66	8.26	7.38	8.04	9.40
Na ₂ O	2.62	2.32	2.17	2.50	3.34	2.40	2.48	2.49	2.82	2.17	3.03	2.41
K ₂ O	1.32	0.87	1.08	0.89	1.20	1.28	1.81	0.88	1.96	1.48	1.32	0.55
P ₂ O ₅	0.47	0.59	0.34	0.35	0.21	0.20	0.67	0.08	0.36	0.49	0.59	0.32
LOI	1.12	1.10	3.24	2.00	1.60	0.40	2.52	0.95	2.36	1.12	1.19	2.10
Total	99.3	99.4	99.0	99.8	99.8	99.6	103.4	98.7	101.0	97.4	100.2	101.9
Mg#	0.33	0.38	0.42	0.50	0.32	0.55	0.54	0.45	0.56	0.32	0.39	0.41
Ba	695	450	600	593	278	356	1015	222	582	576	633	215
Cu	51.00	62.40	0.00	0.00	179.90	120.40	104.00	287.00	120.70	76.70	63.90	502.10
Ni	19.00	45.80	42.00	105.00	11.40	68.50	80.80	8.90	95.40	17.00	33.00	58.00
Rb	41.80	21.50	91.00	68.20	40.60	42.00	63.60	19.20	55.50	59.80	45.30	16.20
Sr	415.90	215.70	0.00	480.30	210.90	410.30	1128.00	477.00	1176.00	676.60	496.20	222.70
Y	37.99	54.16	0.00	23.50	39.40	20.70	16.00	20.00	13.19	0.00	0.00	0.00
Zr	142.90	307.00	104.00	114.40	151.30	103.10	109.20	100.60	102.10	190.90	320.20	259.80
Th	3.90	3.50	2.50	1.60	3.50	1.00	1.30	1.60	2.10	6.00	3.90	3.40
Hf	3.79	6.44	3.30	2.00	4.00	1.90	1.65	2.25	2.01	5.38	7.07	0.00
Cs	3.03	0.97	3.80	7.80	1.60	0.50	1.79	1.32	1.39	17.04	3.53	0.60
Nb	7.60	15.41	7.10	1.70	10.50	4.40	5.23	6.49	2.69	15.14	15.83	12.14
Ga	23.50	22.50	0.00	18.30	20.80	17.10	22.30	27.00	17.10	24.40	24.30	0.00
Ta	1.50	0.79	0.15	0.00	0.30	0.20	0.26	0.13	0.18	1.45	0.97	0.63
U	0.71	0.78	0.83	0.06	0.80	0.60	0.11	0.13	0.51	0.73	0.68	0.44
La	28.60	38.60	21.00	11.20	17.00	11.70	15.50	16.20	14.50	28.20	23.90	17.40
Ce	57.00	64.00	45.00	26.10	38.00	26.90	32.30	36.30	31.90	59.50	53.60	40.50
Pr	7.04	7.27	4.23	3.71	5.06	3.88	4.56	5.25	4.14	7.64	7.12	5.88
Nd	31.10	38.70	24.00	16.30	21.90	18.10	18.70	23.00	18.50	33.10	32.50	27.60
Sm	6.60	8.70	5.00	4.10	5.25	3.90	3.80	4.80	3.50	6.80	8.70	7.60
Eu	2.10	3.27	1.50	0.00	1.62	1.14	0.95	1.14	1.24	2.14	3.24	2.28
Gd	7.40	9.75	0.00	4.15	5.88	3.80	3.49	4.47	3.02	6.92	9.40	9.08
Tb	1.13	1.60	0.70	0.76	1.05	0.61	0.48	0.63	0.43	1.03	1.47	1.35
Dy	6.66	9.38	0.00	4.26	6.50	3.50	3.12	4.10	2.44	6.39	8.96	8.75
Ho	1.39	1.85	0.00	0.78	1.35	0.69	0.57	0.79	0.52	1.31	1.80	1.83
Er	4.01	5.45	0.00	2.26	3.71	1.99	1.52	2.09	1.37	3.71	5.02	4.97
Tm	0.58	0.72	0.00	0.31	0.55	0.33	0.25	0.30	0.41	0.52	0.69	0.65
Yb	3.70	5.00	3.00	2.11	3.49	2.05	0.00	0.00	1.20	3.20	4.40	4.30
Lu	0.52	0.68	0.40	0.30	0.52	0.31	0.22	0.31	0.19	0.52	0.68	0.63
La/Sm _{cn}	2.67	2.73	2.58	1.68	1.99	1.85	2.51	2.08	2.55	2.55	1.69	1.41
Gd/Yb _{cn}	3.86	3.96	0.00	2.70	2.89	3.08	0.00	0.00	4.80	4.08	2.54	1.92
Eu/Eu*	0.92	1.09	0.00	0.00	0.90	0.91	0.80	0.76	1.17	0.96	1.10	0.84
strike	N87E	N85W	N35E							N90W	N88W	N77W

TABLE 2. (Continued)

SAMPLE	TD-101	LM-31A	TD-125	TD-138	LM-82	TD-157	TL100	TL77	TL86
SiO ₂	44.40	45.94	43.80	45.60	46.04	47.20	47.40	47.90	46.30
TiO ₂	3.14	1.53	2.95	2.92	1.44	1.50	2.30	2.96	2.53
Al ₂ O ₃	15.50	15.45	15.60	16.10	15.87	18.10	15.30	14.80	12.60
Fe ₂ O ₃	16.40	14.73	15.60	16.10	13.73	12.20	15.30	17.20	18.80
MnO	0.37	0.22	0.21	0.21	0.20	0.21	0.20	0.22	0.23
MgO	5.27	5.79	5.58	5.97	7.23	5.17	6.10	5.29	9.03
CaO	7.19	8.22	7.79	7.41	9.07	9.91	7.57	7.84	6.58
Na ₂ O	2.76	3.28	3.08	3.48	2.40	2.73	3.18	2.89	2.51
K ₂ O	0.73	1.20	0.82	1.25	0.97	1.16	1.41	1.72	1.54
P ₂ O ₅	0.65	0.69	0.61	0.59	0.51	0.19	0.37	0.61	0.52
LOI	1.12	2.04	1.32	1.14	2.22	1.12	1.20	0.30	0.12
Total	97.5	99.1	97.4	100.8	99.7	99.5	100.3	101.7	100.8
Mg#	0.38	0.43	0.41	0.42	0.51	0.45	0.44	0.38	0.48
Ba	698	750	639	903	760	465	532	699	615
Cu	51.50	0.00	36.30	35.30	0.00	53.90	51.00	66.00	55.00
Ni	85.30	48.00	65.20	68.10	120.00	54.50	104.00	72.00	196.00
Rb	17.40	44.00	27.00	39.80	36.00	29.10	32.90	47.30	44.20
Sr	752.40	0.00	862.40	597.80	0.00	767.40	474.30	304.90	254.80
Y	0.00	0.00	0.00	0.00	0.00	16.33	31.34	44.22	37.31
Zr	184.60	108.90	179.50	174.30	182.00	105.30	184.30	236.60	208.90
Th	2.10	1.10	6.60	2.60	0.50	0.40	2.30	4.70	5.30
Hf	0.00	3.93	5.37	5.00	2.60	0.00	4.56	5.83	5.45
Cs	0.91	0.50	2.88	4.22	1.40	1.31	0.84	1.14	1.53
Nb	16.63	6.40	16.36	15.50	8.20	8.48	10.51	14.41	10.37
Ga	0.00	0.00	22.10	21.60	0.00	0.00	24.40	24.70	20.70
Ta	0.97	0.35	1.15	1.12	1.00	0.26	0.81	0.73	0.49
U	0.34	0.91	0.41	0.38	0.16	0.19	0.71	1.13	1.05
La	28.10	31.00	31.30	24.10	16.00	21.40	20.30	31.70	29.30
Ce	53.70	69.00	66.20	53.00	38.00	36.40	52.50	73.00	64.60
Pr	7.24	6.01	9.13	7.31	5.34	4.28	7.02	9.46	8.32
Nd	32.20	39.00	37.80	32.50	21.00	21.80	31.10	40.40	35.40
Sm	7.00	7.30	8.60	7.40	5.30	4.30	7.30	9.10	7.90
Eu	2.68	2.00	2.88	2.81	1.80	1.54	2.22	2.59	2.28
Gd	7.63	0.00	8.82	7.30	0.00	3.86	7.33	9.30	7.98
Tb	1.10	0.55	1.23	1.14	0.53	0.55	1.07	1.41	1.20
Dy	6.23	0.00	7.01	6.22	0.00	3.14	6.29	8.63	7.39
Ho	1.28	0.00	1.34	1.35	0.00	0.62	1.18	1.66	1.45
Er	3.43	0.00	4.07	3.39	0.00	1.61	3.33	4.74	4.17
Tm	0.47	0.00	0.58	0.46	0.00	0.48	0.47	0.69	0.61
Yb	3.40	2.85	3.60	3.20	2.78	1.40	3.00	4.50	3.90
Lu	0.49	0.40	0.62	0.46	0.40	0.19	0.42	0.65	0.56
La/Sm _{em}	2.47	2.61	2.24	2.00	1.86	3.06	1.71	2.14	2.28
Gd/Yb _{em}	3.68	0.00	3.55	3.30	0.00	5.54	2.77	3.41	3.67
Eu/Eu*	1.13	0.00	1.02	1.18	0.00	1.16	0.93	0.87	0.88
strike	N80W	N25E	N74W	N83W	N40E		N85W	N88W	N78W

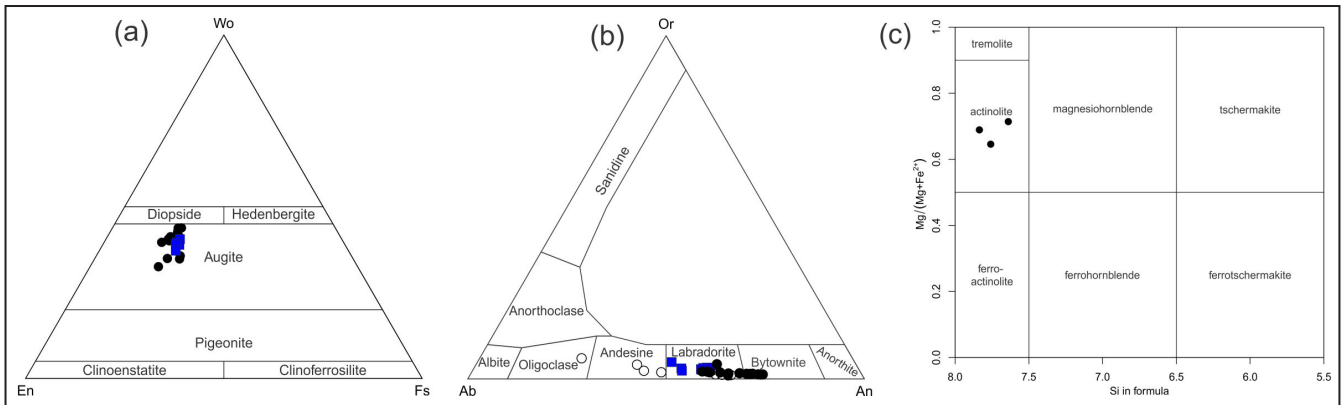


FIGURE 5. (a) Compositional ranges of clinopyroxene plotted on the wollastonite–enstatite–ferrosillite (Wo–En–Fs) diagram. (b) Chemical classifications of plagioclase using the Or–Ab–An diagram. (c) Compositional ranges of Ca-amphiboles based on the Hawthorne et al (2012) classification diagram. Symbols: LTI dikes - black circles; HTi dikes-blue squares; plagioclase crystal rims- hollow circles.

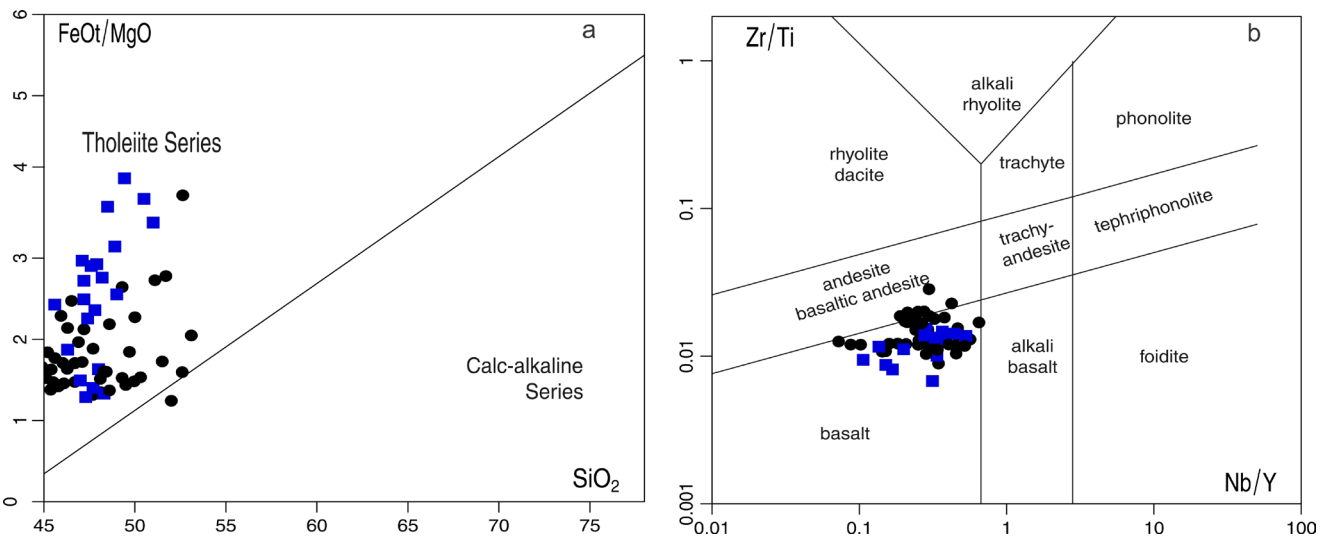


FIGURE 6. Geochemical classification diagrams for the diabase dike swarm of the Juruena-Teles Pires province, based on (a) Miyashiro (1974) and (b) Pearce (1996). Symbols: LTI dikes - black circles; HTi dikes-blue squares.

a dominant role in controlling the chemical evolution of the magma. The multi-element diagram, normalized to chondrites, for dikes from both groups exhibits an enrichment in light rare earth elements (LREEs) and depletion in heavy rare earth elements (HREEs).

The $(La/Yb)_N$ and $(Ce/Yb)_N$ ratios of HTi and LTI dikes range from 2.7 to 12.9 and 1.6 to 10.1, respectively. These ratios, along with the enrichment patterns observed in major and trace elements, are consistent with the differentiation and contamination of the dikes by the surrounding wallrock. Furthermore, most samples exhibit negative Eu anomalies ($Eu/Eu^* = 0.76-1.17$), reflecting plagioclase fractionation and possibly indicating interaction with the continental crust. This trend is expected, as the REE are incompatible with respect to the major crystallizing phases (olivine, clinopyroxene, plagioclase, and magnetite/ilmenite) leading to their progressive enrichment in the more evolved rocks (HTi dikes). Although there is considerable overlap between the two groups, subtle geochemical differences remain observable.

With respect to oxides, for a given Mg#, HTi dikes

are characterized by higher concentrations of TiO₂, FeO_t, K₂O, P₂O₅, and the trace elements such as Zr, Ba, Rb, Ce, La, Pr, Nd and Y. In addition, the HTi diabase dikes exhibit moderate negative Nb, Ta, and Ti anomalies. These and other previously mentioned characteristics suggest crustal assimilation, with the degree of crustal contamination in HTi dikes being proportionally greater than in the LTI group. These LTI dikes show Th depletion, a characteristic often associated with a lower crustal signature, suggesting that the magma was contaminated by lower crust-derived rocks, such as tonalitic and granodioritic gneisses from the Cuiú-Cuiú complex. In this context, the Peixoto de Azevedo domain, which is intruded by LTI diabase dikes, comprises a diverse range of rock types, from granites to more refractory tonalitic and granodioritic rocks. In general, contamination tends to be selective, with rock types rich in alkali feldspar and sodic plagioclase being preferentially assimilated (Huppert and Sparks 1985).

In this sense, and as reported by Puchtel et al. (1998), the assimilation of small amounts of felsic crustal rocks leads to an increased abundance of Ba, Pb, U, Th, and light rare

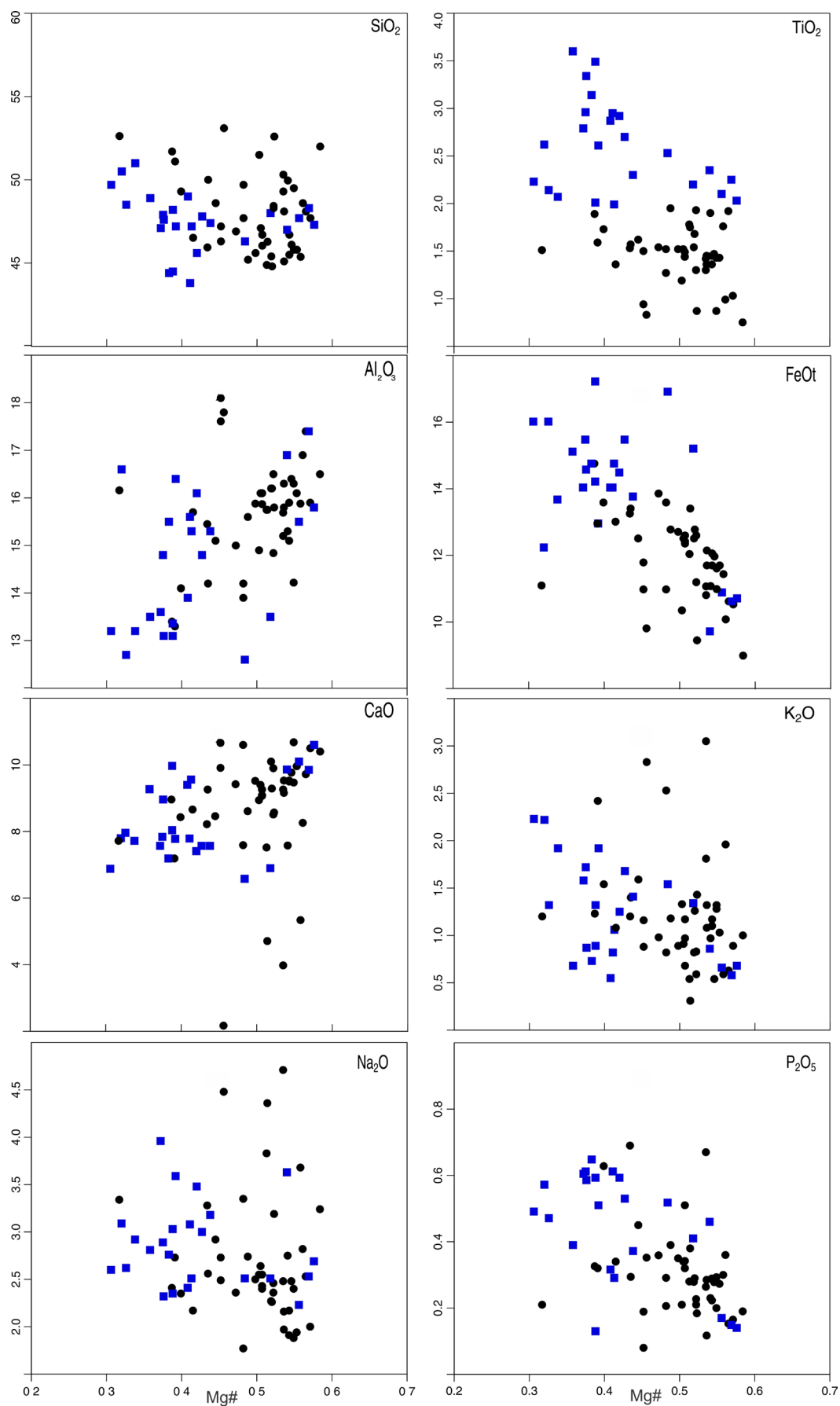


FIGURE 7. a) Geochemical variation diagram for major oxides versus Mg# contents. Symbols are as used in Fig. 5.

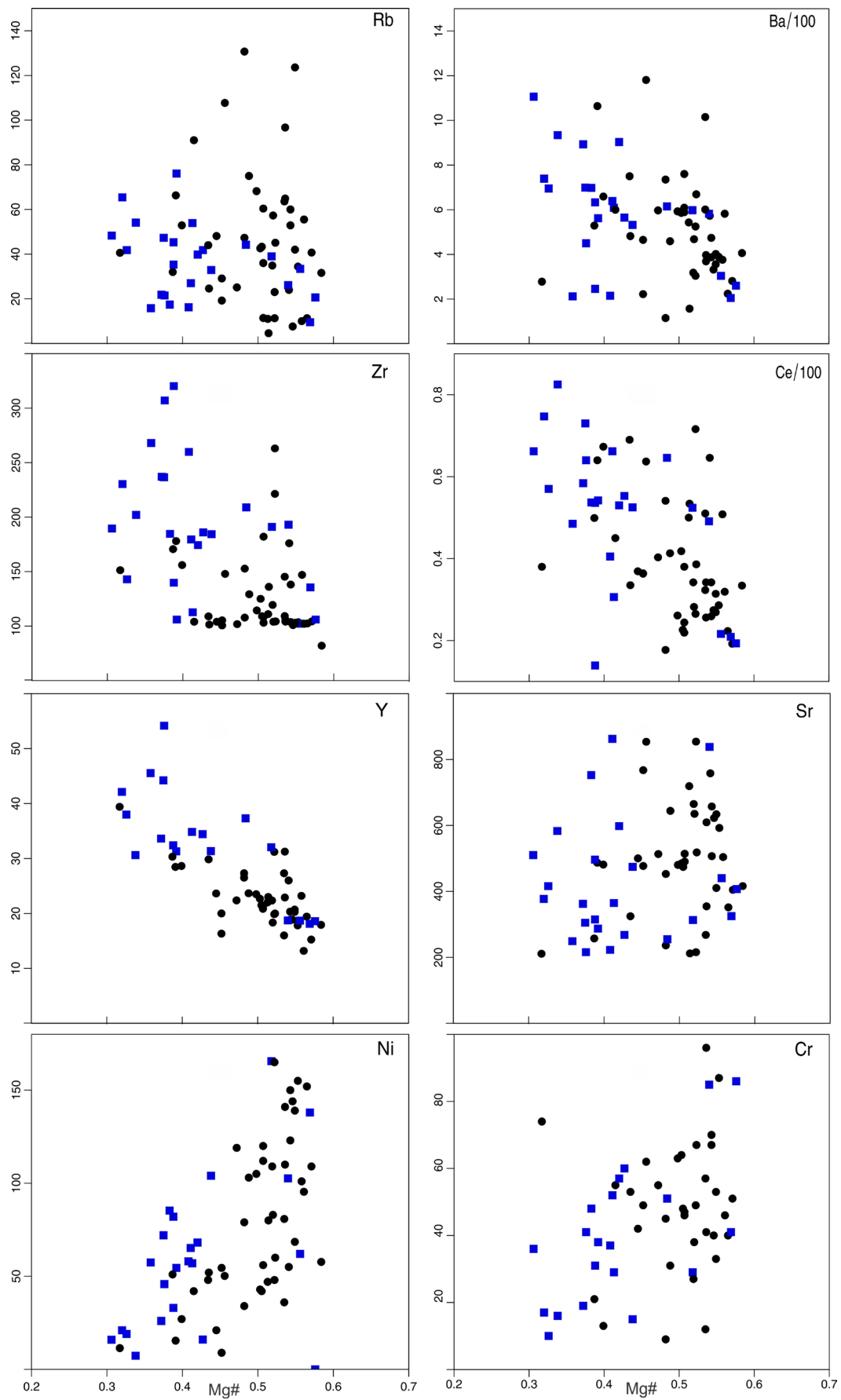


FIGURE 7. b) Variation diagrams for a selected element plotted versus Mg# contents. Symbols as in Fig. 5.

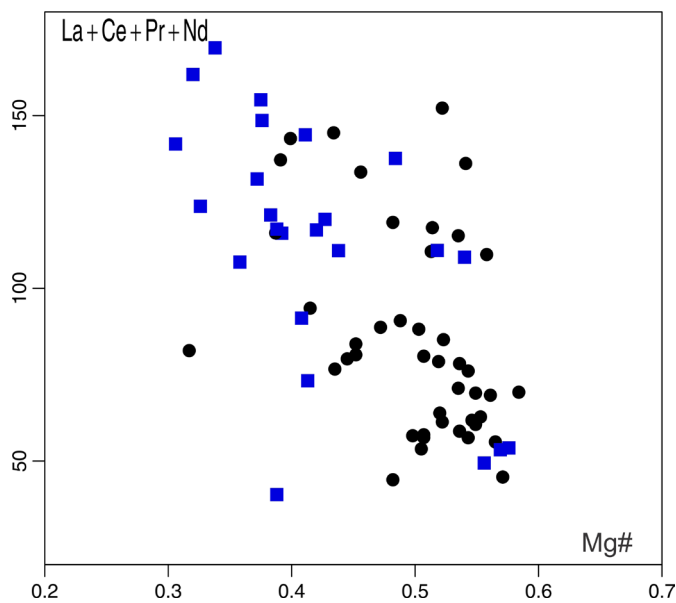


FIGURE 8. LREE vs. Mg# diagram illustrating the geochemical characteristics of high-Ti (HTi) and low-Ti (LTI) diabase dikes.

earth elements (LREEs), while having minimal impact on the concentrations of Ta, Nb, Y, Ti, and heavy rare earth elements (HREEs). This process results in negative Ta, Nb, and Ti anomalies in contaminated rocks. The relationship between typical crustal elements (Ba, Rb, La, Ce, Nb and Ta), as shown in figures 7a,7b, and the spidergram (Fig. 9b) supports the presence of a crustal component in the source of diabase dikes from the Jurueña-Teles Pires mineral province. Similarly, the negative Nb anomaly, combined with positive Th, U, and Rb anomalies, suggests crustal contamination (Thompson 1982). This is also observed in the studied dikes, where the effects of assimilation and crustal contamination are supported by La/Nb ratios ranging from 0.9 to 6.5, which are equivalent to typical crustal values. In addition, REE patterns provide further insights into potential crustal contamination. Contaminated samples typically exhibit significant LREE

enrichment, accompanied by flat or slightly inclined HREE patterns, a characteristic also observed in the diabase dikes of the Jurueña-Teles Pires province (Fig. 9a). To further demonstrate magma contamination by crustal components, we employed ratio-ratio plots, such as Th/Yb versus Nb/Yb, to evaluate the evolution of mantle-derived basic magmas. Figure 10 illustrates these relationships for the diabase dike swarms in the studied region. The data for both groups are displaced almost vertically above the MORB-OIB array (Pearce 2008), positioning them closer to the composition of the lower crust, particularly in some LTI diabase dike samples.

The steep dispersion of dike compositions above the MORB-OIB array suggests significant crust-mantle interaction, resembling the average immobile trace element abundances observed in continental flood basalts (Li et al. 2015). Similar trends are also observed in other immobile incompatible element ratio plots, such as Th/Ta versus La/Yb. Notably, there is considerable variation in Th/Ta and La/Yb ratios between the HTi and LTI dikes. Both groups exhibit very high element ratios, comparable to those characteristic of the lower continental crust, with this signature being particularly evident in some LTI dikes samples (Fig. 11a). The tendency toward elevated Th/Ta and La/Yb ratios in the diabase dikes suggest a moderate degree of contamination by crustal components or, alternatively, mixing of mantle sources. This process could involve a Ta-depleted component (high Th/Ta ratio) interacting with either a plume or a plume-related component in the lithosphere (Condie 1994, 1997).

Rollinson (1993), in turn, emphasized the utility of Ba/Nb, Ba/Zr, and Ti/Y ratios for assessing potential crustal contamination. On the Ba/Zr versus Ti/Y plot (Fig. 11b), most diabase dike samples plot very close to the average lower crust, suggesting a significant role of crustal components in their genesis.

Distinct geochemical differences have been identified between the LTI and HTi diabase dike swarms of the Jurueña-Teles Pires province. These differences may be partially explained by varying degrees of crustal material assimilation. For instance, the HTi WNW-ESE and E-W swarms exhibit enrichments in incompatible elements, suggesting possible crust-magma interactions. However, crustal contamination is

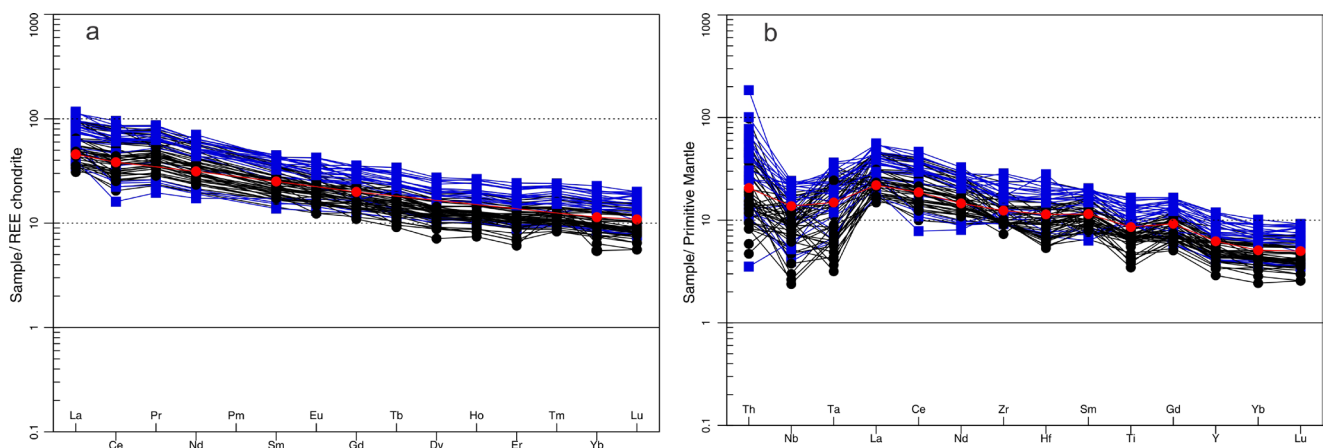


FIGURE 9. (a) Chondrite-normalized REE patterns and (b) primitive mantle-normalized trace element patterns for mafic rocks. Chondrite normalization values are from Nakamura (1974), and primitive mantle normalization values are from Sun and McDonough (1989). Average immobile trace element abundances in continental flood basalts (CFB) are shown for comparison (red circles) (Li et al. 2015).

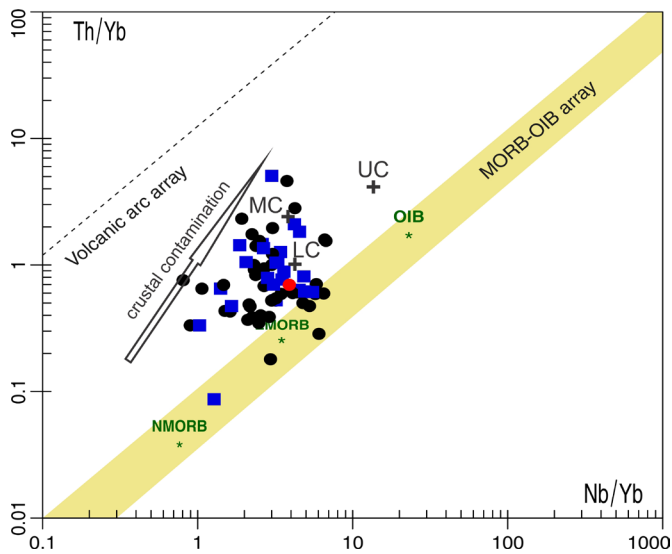


FIGURE 10. Th/Yb versus Nb/Yb diagram (Pearce, 2008) for low-Ti and high-Ti diabase dikes of the Jurueua-Teles Pires Mineral Province. The arrow indicates a crustal contamination trend. Symbols as in Fig. 5. Average CFB (Li et al. 2015) is shown for comparison (red circle). + average lower (LC) middle (MC) and upper (UC) crust (Weaver and Tarney, 1984), * N-MORB (Humphris et al. 1985), * OIB (Sun, 1980), and * EMORB (McDonough et al. 1992).

unlikely to occur without concurrent fractional crystallization, indicating that these two processes are often interconnected in geological settings. In this context, the chemical characteristics of the diabase dike swarms demonstrated in this study are compatible with continental tholeiites. Thus, on the Zr vs. Zr/Y (Fig. 12) tectonic discrimination diagram, the diabase dike swarms of the Jurueua-Teles Pires mineral province exhibit a within-plate basalt signature.

Alternatively, several hypotheses have been proposed to explain the occurrence of high- and low-Ti basalts from the same source. Arndt et al. (1993) suggested that in flood basalt provinces, the occurrence of high- and low-Ti basalts may result from varying degrees of melting of a common mantle source. They proposed that the higher concentrations of incompatible trace elements in high-Ti magmas indicate lower degrees of melting compared to low-Ti magmas. Petrogenetic processes can be identified through ratios of immobile incompatible trace elements, which provide valuable insights into igneous fractionation, including melting and crystallization, within basaltic systems, such as diabase dike swarms (e.g., Condie 1997).

In contrast, Bryan et al. (1977) demonstrated that several mechanisms traditionally proposed to explain the genesis of continental tholeiites—such as variable degrees of partial melting, high-pressure eclogite fractionation, and mantle-wall rock reactions—fail to account for the observed inconsistencies in incompatible element variations, despite the maintenance of relatively similar major and some transition element compositions.

The compositional disparities among continental tholeiites, as well as many of the geochemical differences between them and MORB, particularly the enrichment of Large Ion Lithophile Elements (LILEs) in continental tholeiites, likely result from either crustal contamination or an

enriched subcontinental upper mantle source, both of which may be equally significant in generating these differences. However, constraining the occurrence and extent of crustal contamination in basaltic magmas remains a challenge due to the intricate interplay between assimilation, fractional crystallization, and the geochemical characteristics of the mantle source. This complexity arises because, in certain cases, the geochemical signatures of crustal contamination are nearly indistinguishable from those of magmas derived from a depleted asthenospheric source that subsequently mixed with an ancient continental lithosphere component (e.g., Hooper 1988; Glazner and Farmer 1992; Brandon et al. 1993). Another possible explanation for the geochemical variations observed in continental tholeiitic basalts is the influence of lithospheric mantle contamination. Continental basalts are often enriched in large-ion lithophile elements (LILEs) due to this process (La Flèche et al. 1998). According to Pearce et al. (2021) and Nkouandou et al. (2016), this enrichment can occur during partial melting and/or through assimilation as basaltic magma ascends through the subcontinental lithospheric mantle, which may have been previously metasomatized by earlier subduction events.

Another possible scenario regarding the two groups of dikes is that the LTi dikes exhibit a distinct orientation compared to the HTi dikes. Notably, only the age of the HTi dikes has been constrained, ranging from 1797 to 1773 Ma. Therefore, the LTi dikes may have a different age and originate from a distinct source, which could also account for their compositional differences.

9. Conclusion

This study identified several diabase dikes crosscutting the Archean/Paleoproterozoic basement in the southwestern Amazonian craton. These dikes, distributed within the Peixoto de Azevedo domain and the central-western portion of the Jurueua-Teles Pires mineral province, are classified into two groups based on their TiO_2 concentration: those with TiO_2 content: high-Ti (HTi, >2 wt.%) and low-Ti (LTi, <2 wt.%).

In the Peixoto de Azevedo domain, LTi dikes predominantly follow a NE-SW trend, whereas in the central-western part of the Jurueua-Teles Pires province, HTi dikes intrude Orosirian/Statherian granitic rocks, exhibiting E-W to WNW-ESE orientations and, in some areas, evidence of magma mixing. U-Pb zircon ages (1797–1773 Ma) for HTi dikes (Pinho et al. 2003; Ribeiro and Duarte 2010; Rizzotto et al. 2019) suggest their crystallization and emplacement occurred during a period of intense magmatism and gold mineralization in the Jurueua-Teles Pires province (Assis et al. 2017).

Augite and plagioclase, the latter sometimes exhibiting a Ca-rich core (An_{63-74}) and a Na-enriched rim (An_{26-43}), are the predominant minerals in LTi dikes. Minor phases include Fe-Ti oxides, apatite, and biotite. Hydrothermal alteration products comprise actinolite, chlorite, epidote, Fe/Cu sulfides, white mica, and iron oxides/hydroxides. HTi diabase dikes, in turn, contain labradorite, augite (\pm olivine), magnetite, and ilmenite, with biotite and apatite as common accessory minerals.

The two groups of diabase dikes, HTi and LTi, exhibit typically low Ni contents, which, in conjunction with the observed CaO-MgO correlations, suggest that low-pressure fractional crystallization, predominantly controlled

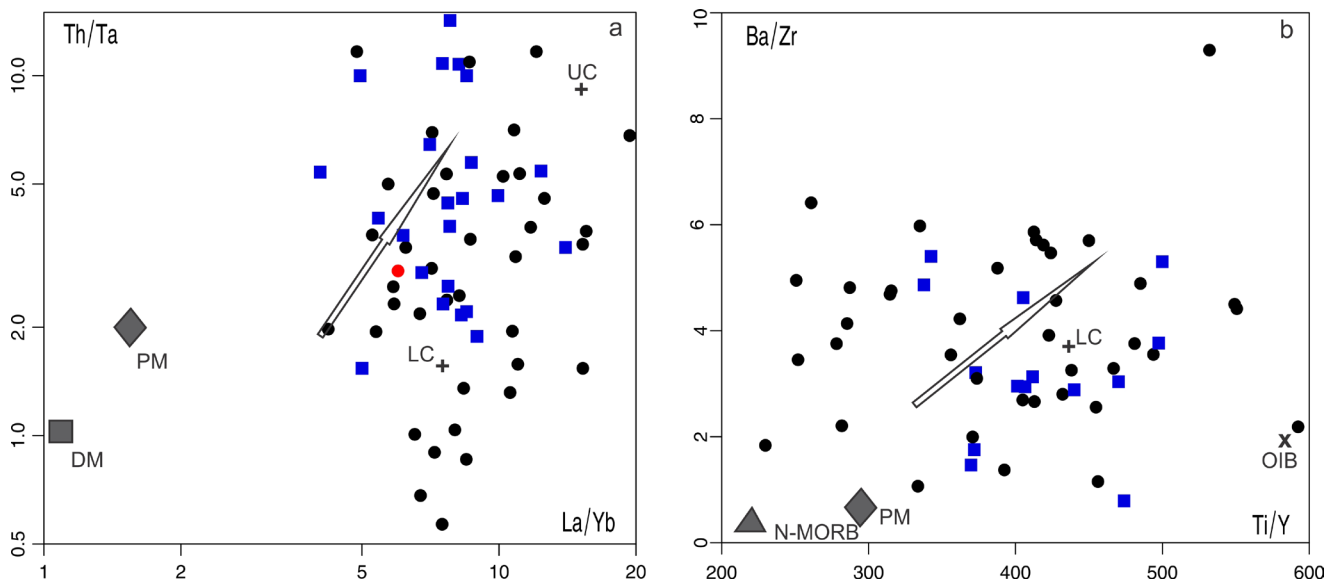


FIGURE 11. (a) Th/Ta vs. La/Yb and (b) Ba/Zr vs. Ti/Y ratio variation diagrams. Symbols are as used in Fig. 5. Other symbols used are: **+** average lower crust (LC) and upper crust (UC) (Weaver and Tarney, 1984), **▲** N-MORB (Humphris et al. 1985), **×** OIB (Sun, 1980), and **◆** PM, primitive mantle (McDonough et al. 1992), **DM**, depleted mantle (McDonough, 1992). Average CFB (Li et al. 2015) is shown for comparison (red circle).

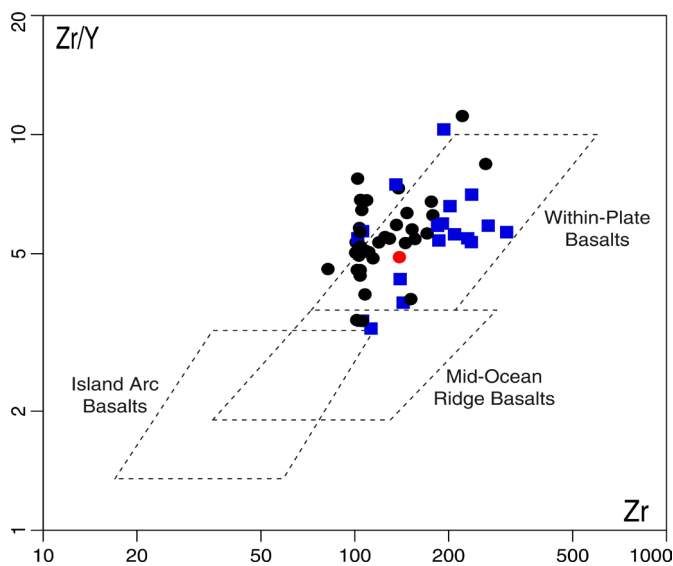


FIGURE 12. Tectonic classification diagram of Pearce and Norry (1979) for mafic dikes swarms. Symbols are the same as in Fig. 5. The average CFB (Li et al. 2015) is shown for comparison (red circle).

by plagioclase and clinopyroxene, was likely. Consequently, these dikes show low to moderate levels of MgO, Mg#, Ni, and Cr levels, indicating that the parent magmas underwent some degree of crystal fractionation and do not represent primary magma compositions. An alternative and coherent explanation for the magmatic evolution of both groups is that the enrichment in K, Ba, Rb, Th, U, La, Ce, and Nd, along with the negative Nb and Ta anomalies, may be indicative of crustal contamination. In this context, the HTi and LTi dikes are tholeiitic in nature, with composition ranging from basalt to basaltic andesite, and are classified as continental flood basalts.

The HTi diabase dikes are slightly more evolved than the

LTi diabase dikes. For a given Mg# value, they are more enriched in TiO_2 , P_2O_5 , Ba, Rb, Sr, Y, Zr, as well as LREEs and HREEs, and exhibit weak positive anomalies of Th, La, Ce, and Nd. The LTi dikes, in diagrams normalized to the primitive mantle (Sun and McDonough 1989), show moderate negative anomalies of Nb, Ta, and Ti, along with weak positive anomalies of Th, La, Ce, and Nd. They also display slightly larger negative anomalies of Ti and Nb compared to the HTi dikes. The geochemical variations between the LTi and HTi groups result from fractional crystallization and crustal contamination, which modified magma composition during its ascent. Alternatively, these differences may partly reflect variations in the degree of melting from the same source, influenced by the presence of a thin crust, which facilitated the development and persistence of convective systems in the upper mantle.

The ~1.80 Ga fissure-controlled HTi diabase dike swarms were emplaced along shear zones and fault systems with predominant orientations ranging from N70W to E-W. In contrast, the LTi dikes that cross-cut the Peixoto de Azevêdo domain, trending N30-50E, are younger than 1.87 Ga (the age of the Matupá granite, which they intrude) and may also include even younger generations. Accordingly, compared to the HTi dikes, the LTi dikes appear to have a different age and originate from a distinct source, which may also explain their compositional differences.

The mafic dike swarms are spatially (and possibly temporally) associated with gold mineralization in most deposits within the Jurueña-Teles Pires province. However, this association is interpreted as indirect, with no consensus on the coexistence of gold and the dikes. The widespread occurrence of mafic dikes within the faults or shear zones that control gold ore suggests that significant mantle-derived fluids associated with the diabase dikes, along with ore components, may have contributed to volatile enrichment and gold mineralization. Therefore, this hypothesis warrants further investigation. Moreover, we discuss the implications

of our findings and the significance of the diabase dikes in the geological evolution of the southwestern Amazonian craton, particularly in relation to the processes associated with the attempt of the Columbia (Nuna) breakup supercontinent at the end of the Paleoproterozoic.

Acknowledgements

This paper is an outcome of research from the Juruena-Teles Pires project, conducted by the Geological Survey of Brazil, to which we express our gratitude for its support in fieldwork and access to analytical facilities. We also thank Lenka Baratoux and the anonymous reviewer for their insightful and constructive comments, which greatly improved this manuscript.

Authorship credits

Author	A	B	C	D	E	F
GJR						
CLA						

A - Study design/ Conceptualization
 B - Investigation/ Data acquisition
 C - Data Interpretation/ Validation
 D - Writing
 E - Review/Editing
 F - Supervision/Project administration

References

- Abbott D.H., Isley, A.E. 2002. The intensity, occurrence, and duration of superplume events and eras over geological time. *Journal of Geodynamics*, 34(2), 265-307. [https://doi.org/10.1016/S0264-3707\(02\)00024-8](https://doi.org/10.1016/S0264-3707(02)00024-8)
- Alves C.A., Rizzotto G.J., Rios F. S., Gonçalves G.F. (org.). 2019. Áreas de relevante interesse mineral - Projeto evolução crustal e metalogenia da Província Mineral Juruena-Teles Pires: estado de Mato Grosso. Goiânia, CPRM. (Províncias Minerais do Brasil, 22). Available on line at: <https://rigeo.sgb.gov.br/handle/doc/21324> / (accessed on 10 January 2025)
- Alves C.L., Rizzotto G.J., Rios F.S., Barros M.A.S. 2020. The Orosirian Cuiú-Cuiú magmatic arc in Peixoto de Azevedo domain, southern of Amazonian craton. *Journal of South American Earth Sciences*, 102, 102648. <https://doi.org/10.1016/j.jsames.2020.102648>
- Arndt N.T., Czamanske G.K., Wooden J.L., Fedorenko V.A. 1993. Mantle and crustal contributions to continental flood volcanism. *Tectonophysics*, 223, 39-52. [https://doi.org/10.1016/0040-1951\(93\)90156-E](https://doi.org/10.1016/0040-1951(93)90156-E)
- Assis R.R. 2015. Depósitos auríferos associados ao magmatismo félsico da Província de Alta Floresta (MT), Cráton Amazonico: idade das mineralizações, geoquímica e fonte dos fluidos. PhD Thesis, Instituto de Geociências, Universidade Estadual de Campinas, Campinas, Brasil, 363 p. <https://doi.org/10.47749/T/UNICAMP.2011.808405>
- Assis R.R., Xavier R.P., Creaser R.A. 2017. Linking the timing of disseminated granite hosted gold-rich deposits to paleoproterozoic felsic magmatism at Alta Floresta gold province, Amazon Craton, Brazil: Insights from pyrite and molybdenite Re-Os geochronology. *Economic Geology*, 112(8), 1937-1957. <https://doi.org/10.5382/econgeo.2017.4535>
- Bispo-Santos F., D'Agrella-Filho M.S., Trindade R.I.F., Elming S. Å., Janikian L., Vasconcelos P.M., Perillo B.M., Pacca I.I.G., da Silva J.A., Barros M.A.S. 2012. Tectonic implications of the 1419 Ma Nova Guarita mafic intrusives paleomagnetic pole (Amazonian Craton) on the longevity of Nuna. *Precambrian Research*, 196-197, 1-22. <https://doi.org/10.1016/j.precamres.2011.10.022>
- Brandon A.D., Hooper P.R., Goles G.G., Lambert R.St.J. 1993. Evaluating crustal contamination in continental basalts: the isotopic composition of the Picture Gorge Basalt of the Columbia River Basalt Group. *Contributions to Mineralogy and Petrology*, 114, 452-464. <https://doi.org/10.1007/BF00321750>
- Bryan S.E. 2007. Silicic large igneous provinces. *Episodes*, 30, (1), 20-31. <https://doi.org/10.18814/epiuiugs/2007/v30i1/004>
- Bryan W.B., Frey F.A., Thompson G. 1977. Oldest Atlantic seafloor: Mesozoic basalts from western North Atlantic margin and eastern North America. *Contributions to Mineralogy and Petrology*, 64, 223-242. <https://doi.org/10.1007/BF00371513>
- Condie K.C. 1994. *Archaean Crustal Evolution*. Amsterdam, Elsevier; *Developments in Precambrian Geology*, 528 p.
- Condie K.C. 1995. Episodic ages of greenstones: a key to mantle dynamics? *Geophysical Research Letters*, 22(16), 2215-221. <https://doi.org/10.1029/95GL01804>
- Condie K.C. 1997. *Plate Tectonics and crustal evolution*. 4th ed. Oxford, Butterworth/Heinemann, 282 p. <https://doi.org/10.1017/S0016756898328885>
- Ernst R.E., Buchan K.L., Palmer H.C. 1995. Giant dike swarms: characteristics, distribution and geotectonic applications. In: Baer, G., Heimann, A. (eds.). *Physics and Chemistry of Dikes*. Rotterdam, Balkema, 321 p.
- Ernst R.E., Bell, K. 2010. Large igneous provinces (LIPs) and carbonatites. *Mineralogy and Petrology*, 98, 55-76. <https://doi.org/10.1007/s00710-009-0074-1>
- Ernst R.E., Bell, Bleeker W., Söderlund U., Kerr A. 2013. Large igneous provinces and supercontinents: toward completing the plate tectonic revolution. *Lithos*, 174, 1-14. <https://doi.org/10.1016/j.lithos.2013.02.017>
- Glazner A.F., Farmer G.L. 1992. Production of isotopic variability in continental basalts by cryptic crustal contamination. *Science*, 255(5040), 72-84. DOI: 10.1126/science.255.5040.72
- Halls H.C. 2008. The importance of integrating paleomagnetic studies of proterozoic dikes with U-Pb geochronology and geochemistry. In: Srivastava R.K., Sivaji C., Rao N.V.C. (eds.). *Indian Dikes: Geochemistry, geophysics and geochronology*. New Delhi, India, Narosa Publishing House Pvt. Ltd., 1-22.
- Hawthorne F.C., Oberti R., Harlow G.E., Maresch W.V., Martin R.F., Schumacher J.C., Welch M.D., 2012. Nomenclature of the amphibole supergroup. *American Mineralogist*, 97(11-12), 2031-2048. <https://doi.org/10.2138/am.2012.4276>
- Hooper P.R. 1988. The Columbia River Basalt. In: Macdougall J.D. (ed.). *Continental Flood Basalts*, Kluwer, p. 1-33.
- Humphris S.E., Thompson, G., Schilling J.G., Kingsley R.H. 1985. Petrological and geochemical variations along the Mid-Atlantic Ridge between 46°S and 32°S: Influence of the Tristan da Cunha mantle plume. *Geochimica et Cosmochimica Acta*, 49(6), 1445-1464. [https://doi.org/10.1016/0016-7037\(85\)90294-7](https://doi.org/10.1016/0016-7037(85)90294-7)
- Huppert H.E, Sparks R.S.J. 1985. Cooling and contamination of mafic and ultramafic magmas during ascent through the continental crust. *Earth and Planetary Science Letter*, 74, 371-386. [https://doi.org/10.1016/S0012-821X\(85\)80009-1](https://doi.org/10.1016/S0012-821X(85)80009-1)
- Kudo A.M., Weill D.F. 1970. An igneous plagioclase geothermometer. *Contributions to Mineralogy and Petrology*, 25, 52-65. <https://doi.org/10.1007/BF00383062>
- La Flèche M.R., Camire G., Jenner G.A. 1998. Geochemistry of post-Acadian, Carboniferous continental intraplate basalts from the Maritimes Basin, Magdalen Islands, Québec, Canada. *Chemical Geology*, 148(3-4), 115-136. [https://doi.org/10.1016/S0009-2541\(98\)00002-3](https://doi.org/10.1016/S0009-2541(98)00002-3)
- Li C., Arndt N.T., Tang Q., Ripley E.M. 2015. Trace element indiscrimination diagrams. *Lithos*, 232, 76-83. <https://doi.org/10.1016/j.lithos.2015.06.022>
- McDonough W.F., Sun S.-S., Ringwood A.E., Jagoutz E., Hofmann A.W. 1992. Potassium, rubidium and cesium in the earth and moon and the evolution of the mantle of the earth. *Geochimica et Cosmochimica Acta*, 56(3), 1001-1012. [https://doi.org/10.1016/0016-7037\(92\)90043-I](https://doi.org/10.1016/0016-7037(92)90043-I)
- Miyashiro A. 1974. Volcanic rock series in island arcs and active continental margins. *American Journal of Science*, 274(4), 321-355. <https://doi.org/10.2475/ajs.274.4.321>
- Moura M.A., Botelho N.F. 2002. Petrologia do magmatismo associado à mineralização do tipo ouro pórfiro da província aurífera Juruena-Teles Pires (MT). *Revista Brasileira de Geociências*, 32(3), 377-386. Available on line at: <https://ppegeo.igc.usp.br/portal/index.php/rbg/petrologia-do-magmatismo-associado-a-mineralizacao-do-tipo-ouro-porfiro-da-provincia-aurifera-juruenateles-pires/mt/> / (accessed on 7 January 2025)
- Nakamura N. 1974. Determination of REE, Ba, Fe, Mg, Na and K in carbonaceous and ordinary chondrites. *Geochimica et Cosmochimica Acta*, 38(5), 757-775. [https://doi.org/10.1016/0016-7037\(74\)90149-5](https://doi.org/10.1016/0016-7037(74)90149-5)

- Nkouandou O.F., Mefire A.F., Deruelle B. 2016. Petrogenesis modeling of the alkaline volcanism of Ngaoundéré (Adamawa plateau, Cameroon, Central Africa). *International Journal of Biological and Chemical Sciences*, 10(4), 1903-1917. DOI: 10.4314/ijbcs.v10i4.38
- Paes de Barros A.J.P. 2007. Granitos da região de Peixoto de Azevedo – Novo Mundo e mineralizações auríferas relacionadas – Província Aurífera Alta Floresta (MT). PhD Thesis, Instituto de Geociências, Universidade Estadual de Campinas, Campinas, Brasil, 154 p. <https://doi.org/10.47749/T/UNICAMP.2007.404585>
- Pearce J.A. 1996. A User's Guide to Basalt Discrimination Diagrams. In: Wyman, D.A. (eds.). *Trace Element Geochemistry of Volcanic Rocks: Applications for Massive Sulphide Exploration*, Geological Association of Canada, Short Course Notes, 12, 79-113.
- Pearce J.A. 2008. Geochemical fingerprinting of oceanic basalts with applications to ophiolite classification and the search for Archean oceanic crust. *Lithos*, 100(1-4), 14-48. <https://doi.org/10.1016/j.lithos.2007.06.016>
- Pearce J.A., Norry M.J. 1979. Petrogenetic implications of Ti, Zr, Y, and Nb variations in intrusive rocks. *Contributions to Mineralogy and Petrology*, 69, 33-47. <http://dx.doi.org/10.1007/BF00375192>
- Pearce J.A., Ernst R.E., Peate D.W., Rogers C. 2021. LIP printing: use of immobile element proxies to characterize large Igneous Provinces in the geologic record. *Lithos* 392-393. <https://doi.org/10.1016/j.lithos.2021.106068>
- Pinho M.A.S.B., Chemale Jr. F., Schmus W.R.V., Pinho F.E.C. 2003. U–Pb and Sm–Nd Evidence for 178 Ga magmatism in the Moriru Region, Mato Grosso, Brazil: implications for Province boundaries in the SW Amazon Craton. *Precambrian Research*, 126(1-2), 1-25. [https://doi.org/10.1016/S0301-9268\(03\)00126-8](https://doi.org/10.1016/S0301-9268(03)00126-8)
- Puchtel I.S., Arndt N.T., Hofmann A.W., Haase K.M., Kröner A., Kulikov V.S., Kulikova V.V., Garbe-Schönberg C.D., Nemchin A.A. 1998. Petrology of mafic lavas within the Onega plateau, central Karelia: evidence for 2.0 Ga plume-related continental crustal growth in the Baltic Shield. *Contributions to Mineralogy and Petrology*, 130, 134-153. <https://doi.org/10.1007/s004100050355>
- Reis N.J., Teixeira W., Hamilton M.A., Bispo-Santos F., Almeida M.E., D'Agrella-Filho M.S. 2013. Avanavero mafic magmatism, a late paleoproterozoic lip in the Guiana Shield, Amazonian Craton: U–Pb ID-TIMS baddeleyite, geochemical and paleomagnetic evidence. *Lithos*, 174, 175-195. <https://doi.org/10.1016/j.lithos.2012.10.014>
- Ribeiro P.S.E., Duarte T.B. (orgs.). *Geologia e recursos minerais das folhas Rio Guariba SC.20-X-D e Rio Aripuanã SC.21-V.C: escala 1:250.000. Goiânia, CPRM. Available on line at: https://rigeo.sgb.gov.br/handle/doc/11355 / (accessed on 10 January 2025)*
- Rizzotto G.J., Alves C.L., Rios F.S., Aparecida de Sant'Ana Barros M. 2019. The Western Amazonia Igneous Belt. *Journal of South American Earth Sciences*, 96, 102326. <https://doi.org/10.1016/j.jsames.2019.102326>
- Rollinson H.R. 1993. Using geochemical data: evaluation, presentation, interpretation. New York, Longman Scientific and Technical, 352 p.
- Santos J.O.S., Hartmann L.A., Gaudette H.E., Groves D.I., McNaughton N.J., Flecher I. R. 2000. A new understanding of the provinces of the Amazon Craton based on integration of field mapping and U-Pb and Sm-Nd Geochronology. *Gondwana Research*, 3, 453-488. [https://doi.org/10.1016/S1342-937X\(05\)70755-3](https://doi.org/10.1016/S1342-937X(05)70755-3)
- Santos J.O.S., Hartmann L.A., McNaughton N.J., Fletcher I.R. 2002. Timing of mafic magmatism in Tapajós Province and implications for the evolution of the Amazon Craton: evidence from baddeleyite and zircon U-Pb SHRIMP geochronology. *Journal of South American Earth Sciences*, 15(4), 409-429. [https://doi.org/10.1016/S0895-9811\(02\)00061-5](https://doi.org/10.1016/S0895-9811(02)00061-5)
- Santos J.O.S., Van Breemen O.B., Groves D.I., Hartmann L.A., Almeida M.E., McNaughton N.J., Fletcher I.R. 2004. Timing and evolution of multiple paleoproterozoic magmatic arcs in the Tapajós Domain, Amazon Craton: constraints from SHRIMP and TIMS zircon, baddeleyite and titanite U-Pb geochronology. *Precambrian Research*, 131, 73-109. <https://doi.org/10.1016/j.precamres.2004.01.002>
- Srivastava R.K. 2011. *Dike Swarms: keys for geodynamic interpretation*. Heidelberg, Springer-Verlag, 605 p. DOI: 10.1007/978-3-642-12496-9
- Sun S.S. 1980. Lead Isotopic Study Volcanic Rocks from Mid-Ocean Ridges, Ocean Islands and Islands Arcs. *Philosophical Transactions of the Royal Society A*, 297(1431), 409-445. <http://dx.doi.org/10.1098/rsta.1980.0224>
- Sun S.S., McDonough W.F. 1989. Chemical and isotopic systematics of oceanic basalts: implications for mantle composition and processes. In: Saunders A.D., Norry M.J., (eds.). *Magmatism in the ocean basins*. Geological Society, London, Special Publications, 42, 313-345. <https://doi.org/10.1144/GSL.SP.1989.042.01.19>
- Tassinari C.C.G., Macambira M.J.B. 1999. Geochronological provinces of the amazonian craton. *Episode*, 22(3), 174-182. <https://doi.org/10.18814/epiuiugs/1999/v22i3/004>
- Tassinari C.C.G., Macambira, M.J.B. 2004. A evolução tectônica do Cráton Amazônico. In: Mantesso-Neto V., Bartorelli A., Carneiro C. D. R., Brito Neves B. B. (ed.). *Geologia do continente Sul-americano: evolução da obra de Fernando Flávio Marques de Almeida*. São Paulo, Beca, 471-485.
- Teixeira W., Hamilton M.A., Girardi V.A.V., Faleiros F.M., Ernst R.E. 2019. U-Pb baddeleyite ages of key dike swarms in the Amazonian Craton (Carajás/Rio Maria and Rio Apa areas): tectonic implications for events at 1880, 1110 Ma, 535 Ma and 200 Ma. *Precambrian Research*, 329, 138-155. <https://doi.org/10.1016/j.precamres.2018.02.008>
- Thompson R.N. 1982. Magmatism of the British tertiary volcanic Province. *Scottish Journal of Geology*, 18, 49-107. <https://doi.org/10.1144/sjg18010049>
- Wang X., Hou T., Wang M., Zhang C., Zhang Z., Pan R., Marxer F., Zhang H. 2021. A new clinopyroxene thermobarometer for mafic to intermediate magmatic systems. *European Journal of Mineralogy*, 33(5), 621–637. <https://doi.org/10.5194/ejm-33-621-2021>
- Weaver B.L., Tarney J. 1984. Empirical approach to estimating the composition of the Continental Crust. *Nature*, 310, 575-577. <https://doi.org/10.1038/310575a0>